Large-eddy simulation of the urban boundary layer using drag-porosity modeling

Quentin Bucquet, Isabelle Calmet, Laurent Perret, Magdalena Maché

Large-eddy simulation of the urban boundary layer using drag-porosity modelling

Quentin Bucquet[a], Isabelle Calmet[a,b], Laurent Perret[a,b], Magdalena Maché[a,b]

[a]Nantes Université, Ecole Centrale Nantes, CNRS, LHEEA, UMR 6598, F-44000 Nantes, France
[b]IRSTV, FR 2488, F-44000 Nantes, France

Abstract

This work details the assessment of the performance of the drag-porosity model implemented in ARPS (Advanced Regional Prediction System) atmospheric Large-Eddy Simulation (LES) solver for simulating the atmospheric boundary layer developing over the urban canopy with comparison with literature. The f ow within and above an idealized urban canopy consisting of a staggered array of cubes with various packing densities modelled with the drag-porosity approach immersed into a neutral, Coriolis-free atmospheric boundary layer at high Reynolds is investigated. Besides one-points statistics, particular interest was given to the ability of the model to reproduce the turbulent coherent structures and their characteristic scales. A detailed analysis of one-point statistics, one- and two-dimensional spectra and two-point correlation functions revealed the presence of typical structures and features found in wall-bounded turbulent f ows (two-scale behavior in the roughness sublayer, ejections, sweeps, self-similar wall-attached large scale streaky motions, canopy-independent very large scale motions). Further investigation to identify the interaction mechanisms between large and small scales based on spectral f ltering highlighted an interaction mechanism that ressembles an amplitude modulation process, as observed in literature on wall-bounded f ows. These f ndings therefore show that the proposed approach is able to reproduce all the key features of the f ow developing over urban terrain.

Keywords: Atmospheric boundary layer, Drag-porosity, Large-eddy simulations, Turbulent f ows

1. Introduction

The numerical modelling of turbulent transport and mixing processes resulting from the interaction between urban areas and the atmospheric boundary layer (ABL) is of great importance for air quality assessment, micro-climate predictions and more generally for environmental wind engineering and structural design (Blocken 2014; Thordal et al. 2019; Potsis et al. 2023). A wide range of scales, from the large coherent structures of the atmospheric boundary layer to the smaller ones generated within the urban canopy, are involved in the unsteady transfers of mass, heat and momentum. Despite the rapid growth in computing power over the past decades, the simulation of all scales and their dynamical interactions remains an issue when the studied area extends to the entire city. Unsteady approaches such as large-eddy simulations (LES) that solve the f ow characteristics around urban elements are generally limited to the size of a single neighbourhood (Nozu and Tamura 2012; Giometto et al. 2016; Tolias et al. 2018). Considering

Accepted version in Journal of Wind Engineering and Industrial Aerodynamics
https://doi.org/10.1016/j.jweia.2023.105432

the scale of the city makes it difficult to detail all the roughness elements. The main issue of the urban boundary layer simulations is thus to model the unsteady scale interactions in such a way that the high heterogeneity of urban areas and their morphological characteristics can be accounted for without necessarily simulating all the details of the flow within the canopy layer. The main objective of the present contribution is therefore to assess and demonstrate the performance of using a drag-porosity approach to model the urban-canopy influence onto the lower atmosphere. The focus is on the capacity of this approach in a LES atmospheric boundary-layer model to represent the main turbulent flow features within the roughness sublayer (RSL) with varying building packing density.

The development of urban canopy models in mesoscale models was first motivated by the need to properly account for the influence of neighbourhood heterogeneity on turbulent mixing and transport, by avoiding the classical constant-flux layer assumption enforced by the Monin-Obukhov similarity theory and thus representing the mean wind and turbulence over the entire thickness of the urban canopy layer (UCL) (Martilli et al. 2002; Otte et al. 2004; Coceal and Belcher 2004; Santiago and Martilli 2010). The dynamic component of these urban canopy models was inspired by the drag approach initially developed for plant canopies, in which the influence of the vegetation on the flow was modelled through a drag force introduced in the Reynolds averaged momentum equations and proportional to a constant drag coefficient, the plant area density and the square of the mean wind speed (see e.g.Wilson and Shaw 1977). Originally based on the intuition of adding a new term into the Reynolds averaged equations to account for the drag force, the drag model was then justified by later works of Raupach and Shaw (1982), Hiraoka (1993) and Finnigan and Shaw (2008). In particular, the double-averaging method that they proposed yields naturally the appearance of an additional term in the double-averaged momentum equations that can be identified as a drag force term.

As for the unsteady modelling of turbulent flows, the drag force approach applied to plant canopies has been used for many years in LES atmospheric models and has proved its effectiveness to represent the turbulent transfers within and above the roughness sublayer (see e.g. Shaw and Schumann 1992; Yue et al. 2007; Dupont and Brunet 2008a,b; Liu et al. 2016). Similar approaches have been used in the context of the turbulent flow modelling over rough walls, demonstrating the suitability of a quadratic drag forcing to represent the rough-wall influence on the flow (Busse and Sandham 2012; Varghese and Durbin 2020). Finally, Bannister et al. (2021) recently used a drag approach, assuming a constant drag coefficient as in most urban canopy models (see e.g. Coceal and Belcher 2004; Otte et al. 2004), in order to study the pollution transport within urban patches of varying packing density.

However, the extension of the drag model from vegetated to urban canopies is not that straightforward. Unlike forest canopies which are generally considered as a porous medium represented by a vertically distributed foliar density, the urban canopy is composed of large roughness elements whose shape, spacing and arrangement influence the characteristics of the flow in the RSL and overlying boundary layer (see e.g. Cheng et al. 2007; Placidi and Ganapathisubramani 2015; Perret et al. 2019). These geometrical parameters are usually represented by the frontal density λ_f (defined as the ratio of the sum of windward area of the roughness elements to the total surface area) and the packing density λ_p (defined as the plan area occupied by the buildings relative to the total surface area). Through the compilation of results from laboratory and field experiments, Grimmond and Oke (1999) highlighted the primary

importance of those parameters on the aerodynamic properties of the urban areas and the link with the three flow regimes identified in Oke (1988): an isolated roughness flow regime for sparse canopies, a wake-interference regime for intermediate densities and a skimming flow regime for dense canopies. Each of these regimes influences not only the bulk flow parameters, but also the development of turbulent structures within the canopy and the interactions with the overlying layer.

Studies of flows over rough walls conducted via cube resolving numerical simulations (Coceal et al. 2007; Kanda 2006), wind tunnel experiments (Castro et al. 2006; Blackman and Perret 2016; Basley et al. 2019) and field experiments (Inagaki and Kanda 2010) have shown that above the RSL, these flows present the same organization as the flows over smooth wall. It has been indeed shown that they are populated by the same type of coherent structures, namely near-wall streaks and large self-similar attached eddies as in Perry and Marušić (1995), large-scale motions (LSMs) and meandering very-large scale motions (VLSMs) composed by low-momentum alternating with high-momentum narrow regions elongated in the streamwise direction as in Marusic et al. (2010), and non-linear interactions between large-scale momentum regions and near-wall structures through an amplitude modulation mechanism as in Mathis et al. (2011). However, important differences were observed due to obstacle-induced turbulence, which depends on the canopy-flow regime. In particular, Coceal et al. (2007) demonstrated the existence of ejection and sweep events responsible for most of the intermittent exchange of momentum between the urban-like canopy flow and the overlying layer as they are major contributors to the Reynolds shear stress. The strong shear layers that form along the top of the obstacles were evidenced by Castro et al. (2006) who observed a coexistence of two energetic scales in the RSL, the obstacle-induced small scales superimposing with the larger scales dominating the overlying layer, and referred to as a "two-scale" behavior. Using laboratory measurements of flow over various rough walls, Placidi and Ganapathisubramani (2015) performed a proper orthogonal decomposition (POD) that evidenced the existence of self-similar behavior of the most energetic modes, therefore confirming the independence of the largest scales from the roughness elements, but a morphology-dependent behavior when considering only the RSL.

Therefore, to accurately represent the unsteady flow over an urban canopy, the parameterization of the drag force model must be adapted to account for the influence of the morphological characteristics. The urban-like canopies consisting in staggered arrays of cubes are considered here since this configuration has been thoroughly studied both experimentally and numerically by means of obstacle-resolving RANS (Santiago et al. 2008), LES (Kono et al. 2010) or direct numerical simulation (DNS) (Leonardi and Castro 2010). All of these studies reported significant variations with height of the local drag force (and hence sectional drag coefficient) and its dependency on packing density λ_p (similar to λ_f in this case) that can be explained by the associated flow regimes. As discussed later by Castro (2017), the mean velocity profile within the urban canopy is not universal : it clearly differs from exponential profiles generally assumed in urban canopy layer models and this is to be related to the drag coefficient profiles. Maché et al. (2010) proposed for the first time a drag model suitable for the large-eddy simulation of the urban boundary-layer (see also Maché 2012). The improvement over vegetation canopy models and current urban canopy models comes from the

use of a vertically distributed drag coefficient that also depends on building density. The sectional drag coefficient was deduced from the tendencies reported in the literature for various densities representative of the three flow regimes to ensure that the mean velocity profiles within the canopy layer were in agreement with those from obstacle-resolving simulations or experiments. This drag approach implemented in the LES atmospheric model ARPS (Advanced Regional Prediction System) is used and investigated in the present study.

In order to demonstrate the ability of our drag-porosity approach to simulate, without any forcing other than that imposed through the drag coefficient and canopy density, the turbulent exchanges between the urban canopy and the overlying layer and the scales characteristic of the RSL, three canopy configurations are considered with packing densities of 6.25%, 25% and 44% in order to cover the three flow regimes reported by Oke (1988). The study focuses on the characteristics of the flow in the RSL above the canopy and in the overlying boundary layer. No direct comparison or analysis of the flow within the canopy will be shown as, by essence, individual buildings and the associated flow feature are not represented by the drag-porosity approach.

The objectives of this paper are : (*i*) to assess the capacity of the drag-porosity model to simulate urban turbulent flows in the roughness sublayer and the log-layer based on comparisons with literature; in particular, the existence of typical turbulent structures found in smooth- and rough-wall flows will be assessed, and (*ii*) to evaluate whether or not the model reproduces the impact of geometrical features on turbulence in the RSL and log-layer.

Section 2 is dedicated to the description of the atmospheric numerical solver ARPS and the drag model used in this study. The results are given in Sect. 3, presenting a first characterisation of the boundary layer, a qualitative visualisation of flow structures via instantaneous snapshots, an investigation of the spectral content, complemented with a two-point correlations analysis, and an analysis of the inter-scale interaction mechanisms existing in the RSL through spectral filtering. Finally, conclusions are given in Sect. 4.

2. Methods

2.1. Model description

The code ARPS (Xue et al. 2000, 2001) used in this study is a 3D atmospheric LES model developed by the Center for Analysis and Prediction of Storms (CAPS, University of Oklahoma) which can be used for mesoscale simulations at high resolution.

The non-hydrostatic compressible filtered Navier-Stokes equations are solved in terrain-following coordinates. The subgrid scale (SGS) momentum fluxes are modelled by solving the SGS turbulent kinetic energy (e) equation. Fourth-order horizontal and second-order vertical momentum and scalar advection schemes are used. Time integration is performed using a leapfrog method of second order for the non-acoustic wave modes (with times steps Δt),

while acoustic waves are integrated with smaller time steps, using a mode-splitting technique.

The present simulations are performed under neutral atmospheric conditions so that moisture, water, snow and ice physics as well as heat transfers are disregarded and the associated conservation equations are not presented here. For the sake of clarity, the equations are presented in Cartesian coordinates.

Based on the drag force approach introduced in ARPS by Dupont and Brunet (2008b) the momentum equation for the i^{th} component can be written as:

$$\overline{\rho}\left(\frac{\partial \widetilde{u_i}}{\partial t} + u_j\frac{\partial \widetilde{u_i}}{\partial x_j}\right) = F_{C_i} + F_{P_i} - \frac{\partial \tau_{ij}}{\partial x_j} - F_{D_i} \tag{1}$$

where tilde variables are LES-resolved variables and over-barred variables indicate the atmospheric base state that is horizontally homogeneous and constant in time, and satisfies the hydrostatic hypothesis.

The Coriolis force term is denoted by F_{C_i} and the pressure-gradient force term F_{P_i} in equation (1) contains an artificial "divergence damping" term used to attenuate acoustic waves:

$$F_{P_i} = -\frac{\partial}{\partial x_i}\left(\widetilde{p}'' - \alpha\frac{\partial \widetilde{\rho u}_j}{\partial x_j}\right) \tag{2}$$

where double primed variables indicate the deviations from base state values. The damping coefficient α depends on the minimum grid size and the acoustic (small) time step. The pressure is computed by solving equation (3) at each small time step:

$$\frac{\partial \widetilde{p}''}{\partial t} + \widetilde{u_i}\frac{\partial \widetilde{p}''}{\partial x_i} = -\overline{\rho}c_s^2\frac{\partial \widetilde{u_i}}{\partial x_i} + \overline{\rho}g\widetilde{u_i}\delta_{i3} \tag{3}$$

where c_s denotes the sound wave speed. Equation (3) is obtained from the equation of state and continuity equation, neglecting here the contribution of diabatic heating on pressure changes.

The drag force component F_{D_i} introduced in equation (1) as a sink term for momentum is expressed for urban canopies as:

$$F_{D_i} = 0.5\overline{\rho}C_d a_f \widetilde{u_i}\sqrt{\widetilde{u_j}\widetilde{u_j}} \tag{4}$$

where C_d is the drag coefficient and a_f is the frontal density per unit volume defined as the ratio of the total windward area of the obstacles to the volume of fluid in a cell:

$$a_f(z) = \frac{\sum_n l_n \Delta z}{\Delta x \Delta y \Delta z - \sum_n l_n w_n \Delta z} \tag{5}$$

where the summation ranges over all buildings within the considered cell, Δx, Δy and Δz are the longitudinal, transversal and vertical grid sizes, respectively, and l_n and w_n are the individual obstacle's length (normal to the wind direction) and width (in the wind direction). The vertical drag force component is supposed to be small and the drag coefficient

in the vertical direction is set to the constant value of 1. For the horizontal components of the drag force, sectional drag coefficients $C_d(z)$ that depend on packing density are used and will be presented in Sect. 2.2.

The SGS stress τ_{ij} in equation (1) is modelled by:

$$\tau_{ij} = -\overline{\rho}\nu_t\left(\frac{\partial\widetilde{u_i}}{\partial x_j} + \frac{\partial\widetilde{u_j}}{\partial x_i}\right) \tag{6}$$

where the eddy viscosity ν_t is modelled with a velocity scale based on the SGS turbulent kinetic energy e :

$$\nu_t = 0.1 l_m \sqrt{e} \tag{7}$$

The SGS mixing length l_m depends on the grid size. Horizontal (l_h) and vertical (l_v) mixing lengths are distinguished in ARPS to deal with mesh aspect ratios currently used in atmospheric applications ($\Delta z < \sqrt{\Delta x \Delta y}$): l_h is considered as $\sqrt{\Delta x \Delta y}$ while l_v is set as Δz. In the present application, the horizontal mesh is of the order of a few meters maximum while the vertical stretching induces vertical grid size ranging from one meter within the canopy to hundred meters near the top of the boundary layer. To avoid discrepancies when the mesh is such that $\Delta z > \sqrt{\Delta x \Delta y}$ (*i.e.* far from the canopy layer) $l_v = l_h = \sqrt{\Delta x \Delta y}$ is imposed in this case. The SGS turbulent kinetic energy budget equation is expressed as:

$$\frac{\partial e}{\partial t} + \widetilde{u}_j\frac{\partial e}{\partial x_j} = -\tau_{ij}\frac{\partial\widetilde{u_i}}{\partial x_j} + \frac{\partial}{\partial x_j}\left(2\nu_t\frac{\partial e}{\partial x_j}\right) - C_\epsilon\frac{e^{\frac{3}{2}}}{l_\epsilon} - C_d(z)a_f(z)e\sqrt{\widetilde{u_j}\widetilde{u_j}} \tag{8}$$

The terms on the right hand side correspond respectively to the shear stress production, the turbulent transport, the dissipation rate and the SGS energy cascade. This last term, based on the sectional drag coefficient in the horizontal direction, depends on the form drag produced by the canopy elements. The formulation used in ARPS was suggested by Shaw and Schumann (1992) and is similar to the drag term (4) used in the momentum equation (1) for the horizontal components.

2.2. Parameterization of the sectional drag coefficient

In order to complete and adapt the drag force model (4 and 5) to urban-like canopies, the vertical distribution of the sectional drag coefficient C_d must be defined for different canopy densities and flow regimes. The dependency of C_d on morphological characteristics of the canopy has been investigated from a literature review, mainly based on the work of Santiago et al. (2008), Kono et al. (2010), Leonardi and Castro (2010) and Macdonald et al. (2000) for staggered arrays of cubes of height h. It is worth mentioning here that a more sophisticated calibration method of the canopy-drag forcing based on multi-objective evolutionary algorithm has recently been proposed by Li et al. (2020) for RANS computation and by Wang et al. (2023) for LES. Similarly, the present approach could benefit the mean velocity profile modeling techniques such as the analytical model for wind flow in canopies derived by Awol et al. (2022). These types of approach are not addressed here and left for future work.

Simulations using the C_d profiles for $\lambda_p = 16\%$ provided in Santiago et al. (2008), Kono et al. (2010) and Leonardi and Castro (2010) were performed by Maché (2012). The resulting mean streamwise velocity profiles (not shown) differed from each other and from experimental data of Macdonald et al. (2000). In particular the simulations failed to reproduce the variation with height of the velocity vertical gradient (reported for example in Castro 2017). This is certainly due to the vertical resolution used in our model which is well suited to real city applications but induces a smoothing of the velocity gradients. The difficulty of using the values directly deduced from obstacle-resolving methods and the unavailability of C_d profiles in the lower part of the canopy for densities larger than 20% justify the need for a specific parameterization of the sectional drag coefficient.

The proposed parameterisation is therefore based on the analysis of the dependence of C_d on the density reported in the literature with the aim of simulating satisfactory mean velocity profiles in the canopy. In particular the sectional drag coefficient C_d should be dependent on the flow regime. For low densities, C_d is nearly constant which correspond to an isolated roughness flow regime. The values of C_d should increase with λ_p (and λ_f) especially in the lower part of the canopy, as a consequence of the wake interference flow regime. For greater densities, C_d should increase in the upper part of the canopy and decrease again in the lower part which can be interpreted as a consequence of the skimming flow. The values of C_d have therefore been adjusted by a guess-and-check method so that the mean velocity profiles obtained by ARPS agree with profiles from literature for staggered cubes arrays. At the top of the canopy a very small drag term is added in one to three cells in the vertical in order to avoid numerical instabilities and to smooth the transition between the canopy and the upper layer. The C_d profiles for three packing densities are presented in Fig. 1 together with the resulting simulated mean velocity profiles which are compared with wind-tunnel measurements and CFD results based on obstacle resolving methods. Data from literature used for the comparison is described in Table 1.

A relatively good fit of the streamwise velocity profiles obtained with the model used in the same configuration as described in Sect. 2.3 is observed for $\lambda_p = 6.25\%$ and 44% with the results of Cheng and Porté-Agel (2016), Macdonald et al. (2000) and Santiago et al. (2008). The profile obtained at 25% departs slightly from results of Leonardi and Castro (2010) and Castro et al. (2006), but shows good match with Yang et al. (2016). This could be explained by their high ratio $\delta/h \approx 24$, that draws near our ratio (= 100).

2.3. Numerical details

Three-dimensional simulations of the atmospheric flow over homogeneous urban canopies on flat terrain were performed within $280h \times 140h \times 140h$ m^3 domains with $560 \times 280 \times 59$ grid points in the x (streamwise), y (spanwise) and z (vertical) directions, respectively. The urban canopy height is set to $h = 10$ m and remains constant over the simulations, but three packing densities of the urban canopy are considered, $\lambda_p = \{6.25\%, 25\%, 44\%\}$, covering the identified flow regimes (Oke 1988). Here, the packing density is set equal to the frontal area density λ_f as in experimental studies over staggered arrangement of cubes from Basley et al. (2019); Blackman et al. (2019); Perret et al. (2019). Horizontal resolution $\Delta x = \Delta y = 5$ m, vertical resolution of 1 m below $z = 25$ m and vertical stretching

Table 1 Details of the datasets used for comparison. For CP-A, MCS, YSMM and CCR, δ refers to the boundary layer depth. LC's DNS is a channel-flow computation, therefore δ refers to the channel half-height. For SCMB's RANS model, δ is taken to be the domain height.

Method	Author	Acronym	δ/h
LES	Cheng and Porté-Agel (2016)	CP-A	≈ 12
Wind-tunnel	Macdonald et al. (2000)	MCS	10
LES	Yang et al. (2016)	YSMM	≈ 24
Wind-tunnel	Castro et al. (2006)	CCR	7.4
DNS	Leonardi and Castro (2010)	LC	8
RANS	Santiago et al. (2008)	SCMB	4

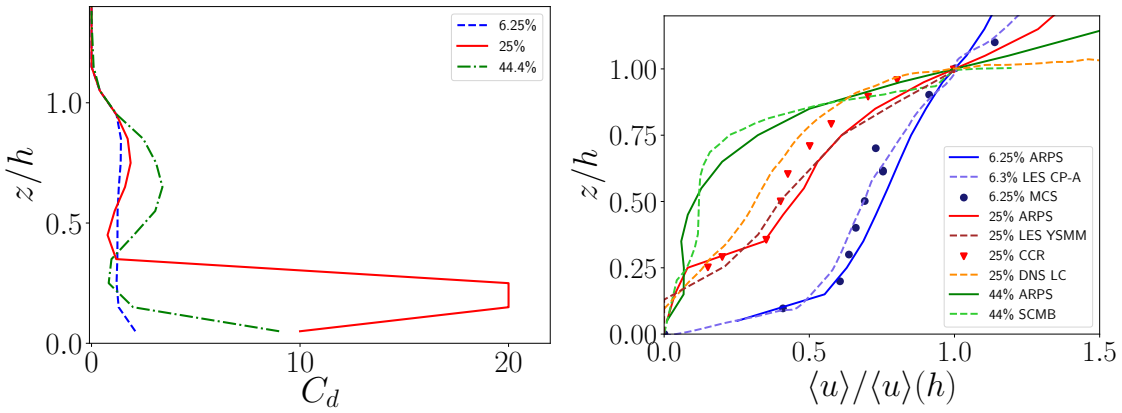

Figure 1 Left : Vertical profiles of C_d for canopy densities $\lambda_p = \{6.25\%, 16\%, 25\%, 44\%\}$. Right : Normalized vertical profiles of the mean streamwise velocity of the present study (solid lines) compared with those of (symbols) wind-tunnel measurements (Macdonald et al. 2000; Castro et al. 2006) and (dashed lines) obstacle resolving methods (Cheng and Porté-Agel 2016; Yang et al. 2016; Leonardi and Castro 2010; Santiago et al. 2008).

as a function of a hyperbolic tangent above were used.

The lateral boundary conditions are periodic, bottom and top boundary conditions are rigid walls and a 400 m deep Rayleigh damping layer is set at the top of the computational domain in order to absorb upward propagating waves and suppress wave reflection from the rigid top boundary. The vertical profiles of the initial velocity field and base-state potential temperature and specific humidity were computed using a meteorological pre-processor (Penelon et al. 2001) with a constant vertical profile of potential temperature 300 K, a dry atmosphere and geostrophic wind of 12 m.s^{-1} aligned with the x-direction imposed at the top of the boundary layer and in the Rayleigh damping layer. No Coriolis force is applied in our simulations as this study aims to compare results obtained from a drag-porosity atmospheric LES model with experimental results obtained from wind tunnel experiments where Coriolis force does not apply. Moreover, the work mainly concentrates on the flow physics in the lower atmospheric boundary layer, a region that does not exceed $z = 300$ m (one third of the ABL depth in the present case), where the veering wind effect remains negligible.

The computation (large) time step was set to $\Delta t = 0.05$s. Since the lowest portion of the ABL is considered in this study, namely the RSL and the logarithmic region or inertial sublayer, the canopy-based turnover time $\tau_r = h/u_*$ is used to assess the statistically steady-state of the dynamic flow field, with u_* the friction velocity. The simulations with a horizontal spatial grid spacing of $\Delta x = h/2 = 5$ m were run for 400 000 time steps for the LES, corresponding to approximately $600\tau_r$, and required approximately 7830 core hours of computational time. Moreover, these simulations were initialized with interpolated converged fields from coarser horizontal resolutions ($\Delta x = h = 10$ m), run for $530\tau_r$. By using this grid interpolation initialization option, we ensure that flow fields quickly reach a statistically quasi-steady state : a time convergence study was performed for each simulation, but is not presented here. The choice of the grid resolution was assessed through a grid convergence study, summarized in appendix A. In order to ensure statistical convergence, we choose to average flow quantities over an averaging period of $400\tau_r$.

In the following, results are consistently presented with regards to the three canopy densities : $\lambda_p = 6.25\%$, 25%, and 44%.

3. Results and discussion

In this section, numerical results obtained with the drag-porosity model for three urban canopy configurations are analysed and compared with experimental results. For the sake of clarity, the tilde symbol used for LES-resolved variables is omitted in the following. The streamwise, spanwise and vertical velocity components will be refered as u, v and w respectively. Each flow variable ϕ is decomposed in a mean and a fluctuating part :

$$\phi = \langle \phi \rangle + \phi' \tag{9}$$

where ϕ is the instantaneous variable, $\langle \phi \rangle$ the (horizontal) space-time average and ϕ' the turbulent fluctuations. The homogeneous description of the urban canopy employed in the present approach allows for the combination of spatial

Table 2 Characteristics of the boundary layers in the three densities

λ_p	u_*	δ/h	δ^+	z_0/h	d/h
-	m s^{-1}	-	-	-	-
6.25%	0.281	100	1.80×10^7	0.087	0.124
25%	0.310	100	1.98×10^7	0.129	0.578
44%	0.284	100	1.82×10^7	0.102	0.847

averaging in horizontal planes with temporal averaging to improve the statistical convergence.

It is worth noting that when the roughness elements are explicitly described, the instantaneous variables (for instance the velocity field u_i) can be decomposed into three components (Coceal et al. 2006) :

$$u_i = \langle \bar{u}_i \rangle_{xy} + u_i' + u_i'' \tag{10}$$

where $\bar{u}_i$ is the time average of the variable u_i at a fixed point, $\langle u_i \rangle_{xy}$ is the spatial average of u_i and $\langle \bar{u}_i \rangle_{xy}$ represents the time-space average of u_i. The component $u_i' = u_i - \bar{u}_i$ is the local turbulent fluctuation relative to $\bar{u}_i$, and $u_i'' = \bar{u}_i - \langle \bar{u}_i \rangle_{xy}$ is the spatial variation of $\bar{u}_i$. The sum $u_i' + u_i''$ is the fluctuation from the time-space average value $\langle \bar{u}_i \rangle_{xy}$. From these definitions, the turbulent stress tensor resulting from time-space averaging is the sum of the spatially averaged Reynolds stress $\langle \overline{u_i' u_j'} \rangle_{xy}$ and the so-called dispersive stress $\langle u_i'' u_j'' \rangle_{xy}$ which represents momentum transport due to spatial variations in the horizontal directions.

Using the drag-porosity approach to model the urban canopy removes spatial heterogeneities in horizontal directions, leading to $\langle \bar{u}_i \rangle_{xy} = \bar{u}_i$ ($\equiv \langle u_i \rangle$ in this work's notation), $u_i'' = 0$ and thus $\langle u_i'' u_j'' \rangle_{xy} = 0$. For this reason, the turbulent stress is only approximated by the space-averaged Reynolds stress $\langle \overline{u_i' u_j'} \rangle_{xy}$ ($\equiv \langle u_i' u_j' \rangle$ in this work's notation) in model-to-measurement comparisons, and the dispersive stress is never accounted for.

3.1. Characterisation of the boundary layer

The flow Reynolds number $\delta^+ = \delta u_* / \nu$ is in between 1.8×10^7 and 1.98×10^7 for the densities considered, where δ is the boundary layer height (Table 2). The friction velocity u^* is estimated from the vertical profile of the Reynolds shear stress in the constant shear stress region, given by :

$$u_* = \frac{1}{h} \int_h^{2h} \sqrt[4]{\langle u'w' \rangle^2 + \langle v'w' \rangle^2} dz \tag{11}$$

The aerodynamic roughness length z_0 and the displacement height d are derived from the logarithmic law :

$$\langle u \rangle = \frac{u_*}{\kappa} \ln\left(\frac{z-d}{z_0}\right) \tag{12}$$

with the von Kármán constant κ set to 0.4.

Both aerodynamic parameters z_0 and d are determined by optimizing the same logarithmic fit of the averaged velocity

profiles so as to minimize the root mean square error fitting.

The present boundary layer shows the existence of an unambiguous log-layer in all investigated cases. This is shown in Fig. 2 where wall-normal profiles of the averaged streamwise velocity component exhibit a log-law similarity over more than an order of magnitude.

The basic properties of the ABL are reported in Table 2. The logarithmic law (12) is only valid within the so-called inertial sublayer that extends above the RSL to the height of the atmospheric surface layer. Thus, as per Fig. 2, the RSL extends up to $(z-d)/z_0 \approx 20$ for the three configurations (*i.e.* $z/h = 1.86$ for $\lambda_p = 6.25\%$, 3.16 for 25% and 2.89 for 44%). This is a typical estimate of the RSL height. For example Ismail et al. (2018) found a similar extent of the RSL up to $2h - 2.5h$ from their Direct Numerical Simulations of cube-roughened walls, while values in the order of 2h-5h are also reported in the literature (Raupach et al. 1991). Additionally, the log-law is valid up to $(z-d)/z_0 \approx 100$, which is $z/h = 8.82$, 13.48 and 11.05 for $\lambda_p = 6.25\%$, 25% and 44% respectively. This is in agreement with the expected values of the atmospheric surface layer depth of about 10% of the atmospheric boundary layer height ($\simeq 10h$ in the present case). A particularly good concordance with experimental results from Perret et al. (2019) of the wall-normal velocity profiles of the three configurations is retained, with similar RSL and log-layer depths, as well as comparable ABL characteristic parameters.

The direct comparison of the aerodynamic parameters with values of previous studies is not straightforward since large scatter is observed (see e.g. Grimmond and Oke 1999 or Figure 3 in Perret et al. 2019) due to measurement accuracy or differences in the method employed to estimate u_* (either from the drag force as in Perret et al. (2019) or from the turbulent shear stress above the canopy as in eq 11) and d (as the height where the drag is acting Jackson 1981 or from the log-law fitting of z_0 and d as in the present study).

The value of z_0 matches well the estimates of Perret et al. (2019) and Macdonald et al. (1998) for the two lowest densities, but is overestimated for the case $\lambda_p = 44\%$. However, the change of z_0 with λ_p is comparable for both results with a larger value of z_0 at 25%.

The value of the displacement length d, which is typically between $0 < d < h$ and given in Table 2, shows good agreement with the range reported by Grimmond and Oke (1999) and Macdonald et al. (2000) for all densities. As expected and reported in literature, the value of d/h increases with increasing λ_p.

The aerodynamic parameters deduced from the present simulations confirm that the drag approach is able to satisfactorily reproduce the bulk influence of the urban canopy on the atmospheric surface layer for various packing density and flow regimes.

Profiles of variances, skewnesses and Reynolds stresses of u and w are shown in Fig. 3. Variances of the streamwise and vertical components show great dependency on packing density, while no clear trend is observed for turbulent shear stress. Variances and Reynolds shear stress are presented alongside profiles obtained by Perret and Rivet (2018) based on stereoscopic PIV over staggered arrays of cubes of packing density 25%. Perret and Rivet (2018) used a

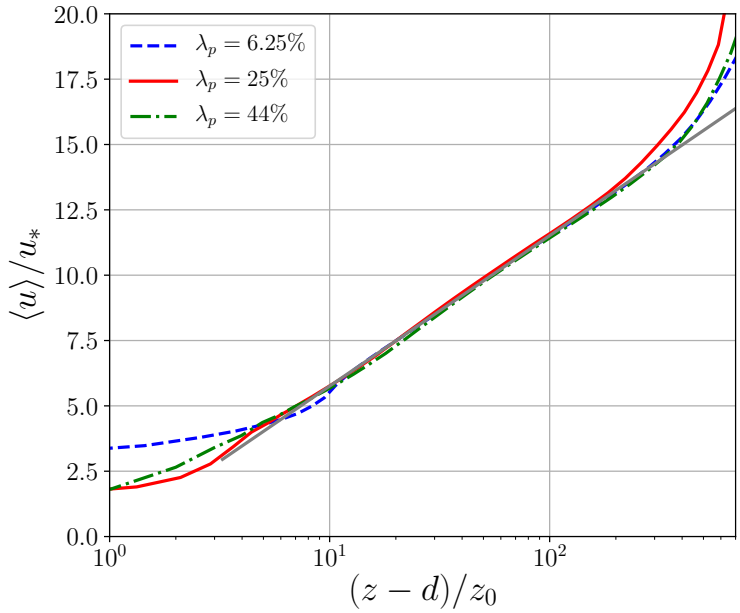

Figure 2 Wall-normal profiles of the mean streamwise velocity component. The solid black line depicts the logarithmic law for the streamwise velocity (equation 12).

double average both in time and in the streamwise direction to smooth out the RSL heterogeneity due to the presence of the obstacles in the canopy. For this reason, the dispersive stress is not considered and only the Reynolds stresses are compared, which show good agreement between numerical and experimental results. Additionally, although the values of the variance of the streamwise velocity component observed in the RSL ($1 < z/h < 2$) are consistent with Perret and Rivet (2018), the vertical profiles does not show a good match above. This could be due to the large differences of ratio δ/h (22.7 in Perret and Rivet 2018, 100 in this study).

The skewness profile of w yields strong negative levels within the canopy and inside the RSL. This result, coupled with strong positive levels of the skewness profile of u in the RSL, underlines the predominant contribution of downward motions with positive fluctuations u' to the Reynolds stresses. Above the RSL ($z/h \leq 2$), upward motions become predominant, while streamwise skewness levels decrease with height. Further results on the dynamic motions in the RSL and logarithmic layer are obtained in 3.2 using a quadrant analysis.

An overall good collapse of velocity profiles with this theoretical log-law and higher order moment profiles with literature confirms the well-developed high Reynolds number character of the investigated flows and suggests that the coherent turbulent structures obtained with the drag-porosity approach can be compared to the commonly accepted view of wall-bounded turbulence. Moreover, this study confirms that the horizontal planes studied in the rest of this paper, located at $z/h = 1.45$ and 4.45 are located in the RSL and the log-layer, respectively, for the three investigated flows.

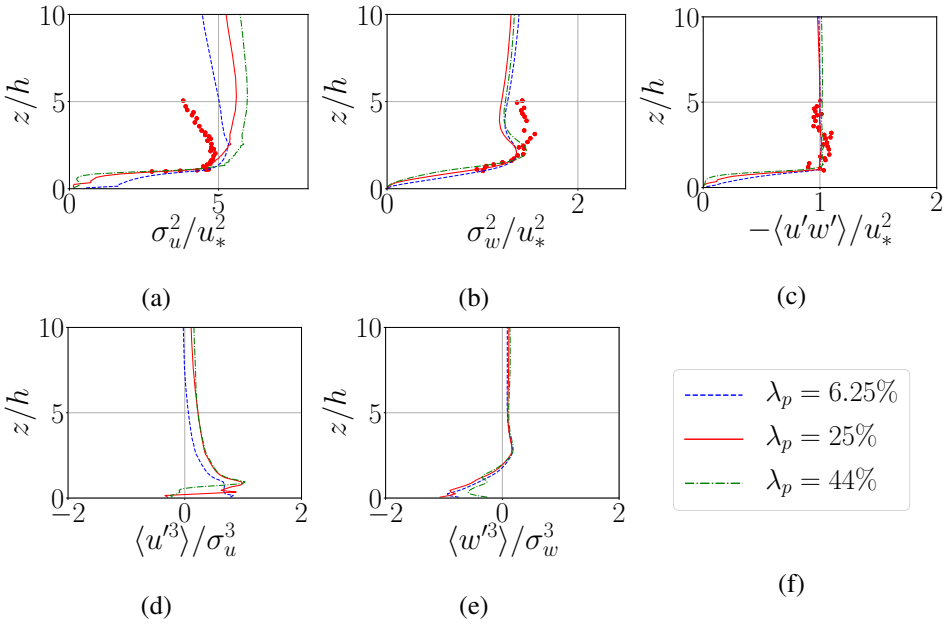

Figure 3 Vertical profiles of variances of (*a*) streamwise and (*b*) vertical components; skewnesses of (*d*) streamwise and (*e*) vertical components; turbulent flux : (*c*) $-\langle u'w'\rangle$. Red dots represent variances and Reynolds shear stress measured from SPIV of Perret and Rivet (2018) over cubic obstacles of density 25%.

3.2. Dynamic motions in the RSL and logarithmic layer

Snapshots of the fluctuating streamwise velocity u'/u_* in top and side views of the last iteration are discussed here for a qualitative analysis. In the side planes presented in Fig. 4, streamwise velocity fluctuations of the three considered flows have similar appearances, and present eddies of approximately similar sizes and intensity levels. A noticeable difference between the packing densities can however be observed in the near-canopy region where an increase in packing density forces streamwise velocity fluctuations to small values.

Figure 5 compares the top views of fluctuating streamwise velocity inside the canopy ($z/h = 0.55$), in the RSL ($z/h = 1.45$) and in the log-layer ($z/h = 4.45$) for the three investigated flows. In the log-layer of each flow configuration, velocity fluctuations exhibit streaky LSMs, elongated in the streamwise direction with a slightly spanwise meandering effect, characteristic of turbulent boundary layers over smooth planes (Hutchins and Marusic 2007), over vegetation canopies (Watanabe 2004), and over cube canopies (Basley et al. 2018). As in Basley et al. (2019), the coherent structures in the log-layer show no apparent dependency on the canopy configuration. In the RSL, u'/u_* exhibits anisotropic structures, showing low- and high-speed streaks elongated in the streamwise direction with locations matching well that of the upper LSMs found at $z/h = 4.45$: these can be seen as the footprints of the upper LSMs. However it should also be noticed that, in the RSL, smaller and weaker structures (of size of the order of h) co-exist and are superimposed onto larger scale structures (of size of the order of δ). This superposition, and the fact that sweeping and ejecting motions highlighted by negative fluctuations of wall-normal shear stress $u'w'$ (black contour lines in Fig. 5(*d*)) are mostly generated by LSMs is in good agreement with results obtained from vegetation canopies

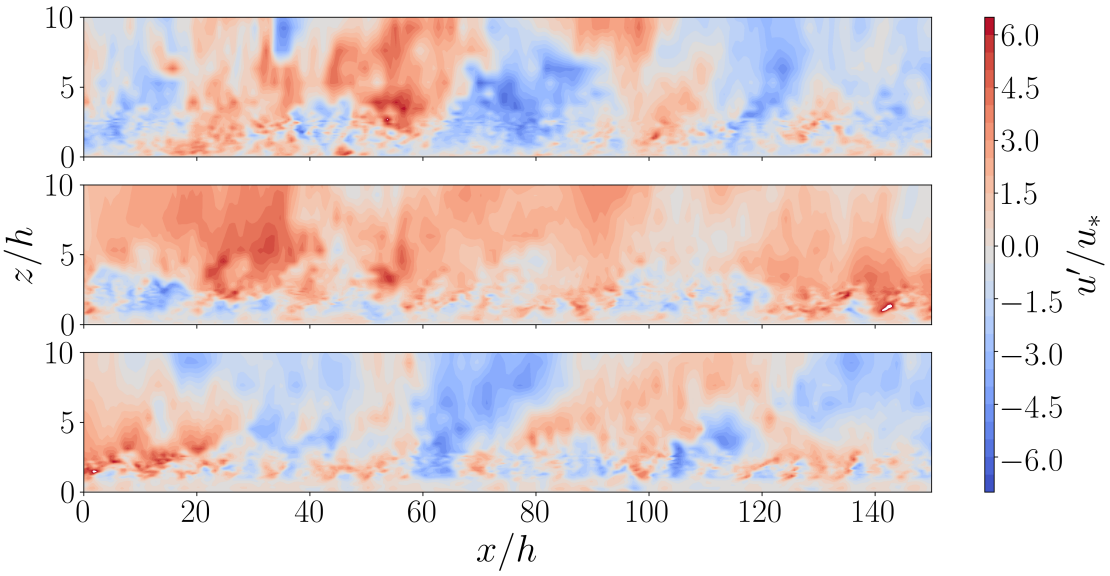

Figure 4 Instantaneous fluctuations of the streamwise velocity component normalised by u_* for $\lambda_p = 6.25\%$ (top), $\lambda_p = 25\%$ (centre) and $\lambda_p = 44\%$ (bottom) in a $x - z$ plane.

(Raupach et al. 1996, Perret and Patton 2021), and from experimental studies over cube canopies (Basley et al. 2019). In the RSL, it appears from Fig. 5 that sweeps, depicted by intense positive fluctuations of streamwise velocity, exist as compact strong packets, while ejections, corresponding to intense negative fluctuations of streamwise velocity are much rarer and weaker.

Additional information on the relative contribution of ejections (Q2) and sweeps (Q4) events is given by the skewness profiles in Fig. 3(d, f) and the quadrant analysis showed in Fig. 6. As expected, the contribution of Q1 and Q3 events to the Reynolds stress is small compared to the more significant contribution of Q2 and Q4 events. The three packing densities considered exhibit similar dynamic motions structure within the RSL : an overall larger contribution of downward events with positive u' fluctuations to the Reynolds stress (sweep events) inside the canopy, which peaks at $z/h = 1$, and a predominant contribution of upward events with negative u' fluctuations (ejection events) above the canopy height with an inversion point located at $z/h \approx 1.6$ for 6.25%, 1 for 25% and ≈ 1.2 for 44%. This inversion between Q4 and Q2 events contributions is in good agreement with the work of Coceal et al. (2007) and Castro et al. (2006) from DNS and wind tunnel experiments of a staggered cube array respectively. Indeed, they found that close to the obstacles sweeps contributed more to the mean shear stress than ejections, while away from the wall the opposite was found. Additionally, they located the crossover point between sweep and ejection dominance at $z/h = 1.25$. The packing density appears to have an impact on the predominating events inside the canopy : while a clear predominance of Q4 events is observed throughout the canopy for 6.25%, it is less true for denser canopies where Q2 events even appear predominant for $z/h < 0.5$ for 44%. However, such a feature is difficult to interpret and could be unrealistic.

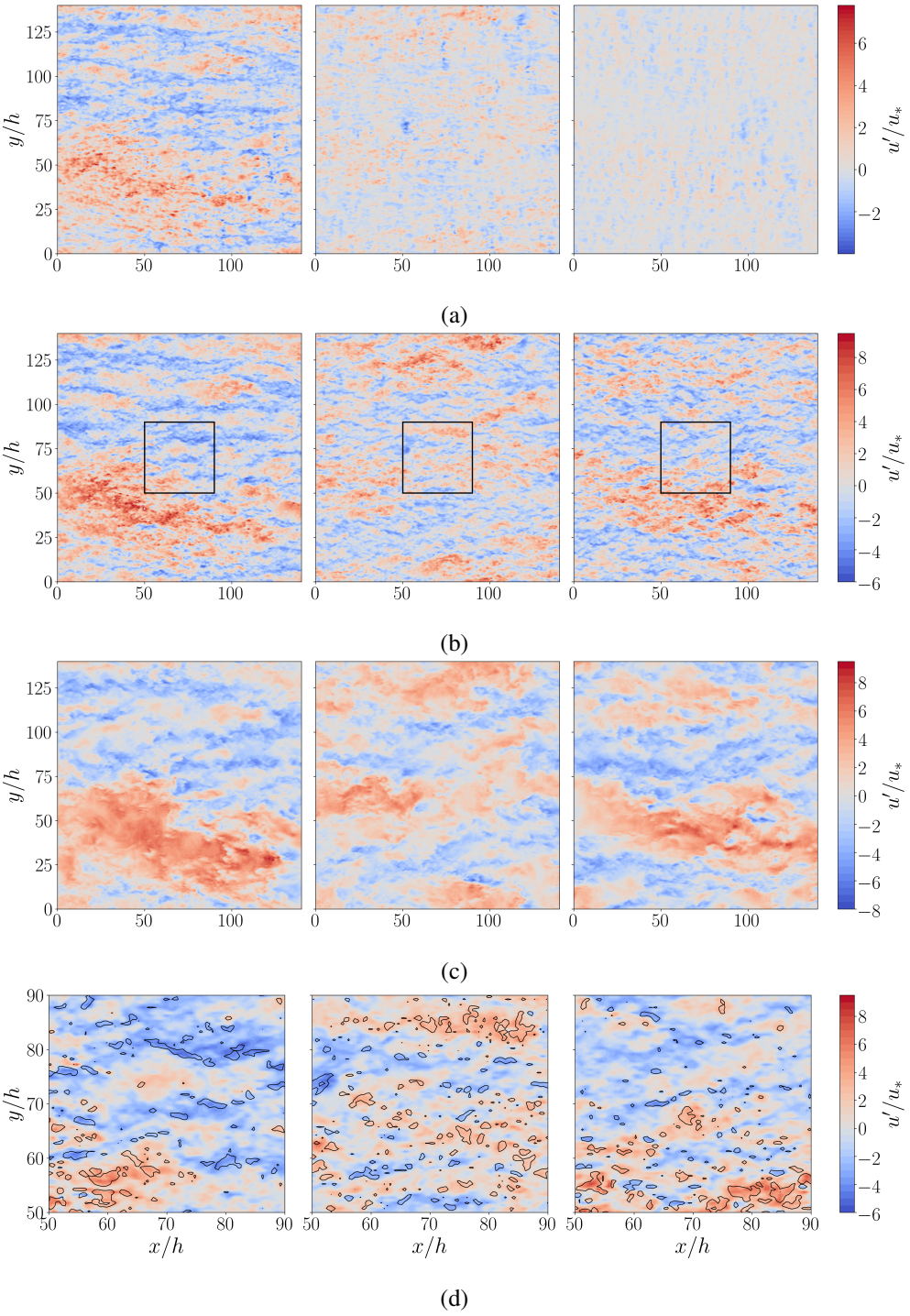

Figure 5 Instantaneous fluctuations of the streamwise velocity component normalised by u_* for $\lambda_p = 6.25\%$ (left), $\lambda_p = 25\%$ (centre) and $\lambda_p = 44\%$ (right) in a $x-y$ plane at : (*a*) $z/h = 0.55$, (*b*) $z/h = 1.45$, (*c*) $z/h = 4.45$. Panels (*d*) are close-up views of the centre of the velocity field at $z/h = 1.45$ corresponding to the black squares shown in (*b*). Solid black contour lines depict intense negative levels of wall-normal shear stress $u'w'$ at level $-9.12u_*^2$.

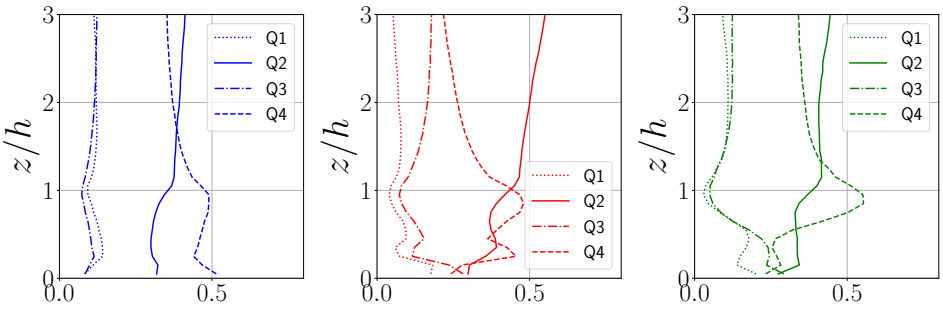

Figure 6 Relative contribution to $\langle u'w' \rangle$ of events in each quadrant for packing densities of 6.25% (a), 25% (b) and 44% (c).

Even if this work does not aim at characterizing the turbulent structures and their interactions inside the canopy, interesting results can be highlighted from plots in Fig. 5 at $z/h = 0.55$. Firstly, a striking effect of the canopy configuration concerns the difference in momentum levels between the three canopy configurations. Indeed, an isolated regime at $\lambda_p = 6.25\%$ enables more intense velocity fluctuations, while the wake-interference and skimming flow regimes ($\lambda_p = 25\%$ and 44% respectively) tend to block the development of low- and high-momentum structures. Additionally, the footprint of LSMs seen in the RSL extend down to low levels (typically $z/h = 0.55$) in the isolated flow regime, as a result of the penetration of the shear layer inside the canopy (in good agreement with Oke 1988). However, in denser canopies, the influence of LSMs inside the canopy is weaker, and smaller structures scale with h. Another interesting result from these top views concerns the elongated streak sizes broken down with canopy density, and is to be link with Varghese and Durbin (2020) who investigated three flow configurations: a smooth-wall model, a rough-wall model (equivalent to the drag-porosity model presented here) and a cube resolved model. By observing a break down of streaks inside the canopy for both roughness and cube resolved models compared to the smooth model, they conclude that streaks breaking down is not a result of physical obstruction of cubes, but of drag alone. A similar result is obtained here when comparing the isolated flow regime (relatively close to a smooth model) with denser canopies.

3.3. Spectral content

The qualitative conclusions based on the instantaneous velocity fields in Sect. 3.2 are now further investigated through a spectral analysis aiming to identify the structuring length scales of the flow, from the small-scale canopy-induced dynamics to the LSMs and VLSMs developing in the logarithmic layer and above respectively. In the following, one-dimensional spectra are identified with a single subscript, *i.e.* S_x for an auto-spectra in the x-direction, whereas their two-dimensional counterparts are referred to as S. All spectra presented in Fig. 7 - 10 are pre-muliplied by wavenumbers $k_{x,y} = 2\pi/\lambda_{x,y}$.

Figure 7 shows $S_x(u,u)$ and $S_y(u,u)$ the pre-multiplied one dimensional spectra of u as a function of wall-normal distance z/δ and streamwise and spanwise wavelength λ_x and λ_y, respectively, as well as the location of the local maximum of the spectra. When considering the evolution of the wavelengths corresponding to the maximum of energy with height in the streamwise and spanwise spectra of u, three distinct regions appear.

Within the canopy, the location of local maximum is approximately constant with height and correspond to similar wavelength for streamwise and spanwise spectra : $\lambda_{x,y}/h \approx 10$. This behavior is observed for the three configurations and relatively small energetic levels are reached inside the canopy. However a noticeable difference between energetic levels inside the canopy can be pointed out : the denser the canopy, the smaller the energetic level.

Above the canopy, for the RSL and the lower part of the log-layer (*i.e.* $1 \times 10^{-2} < z/\delta < 5 \times 10^{-2}$), the spectrograms of u depict a shift of maximum energy with wall-normal distance z/δ towards larger scales. For the streamwise direction, this region has to be divided into the RSL ($1 \times 10^{-2} < z/\delta < 3 \times 10^{-2}$), where the wavelengths corresponding to the near-canopy structures increase with the wall distance either as $\lambda_x \propto z^2$, and the lower part of the log-layer ($3 \times 10^{-2} < z < 5 \times 10^{-2}$), where the ridge of maximum energy follows a self-similar tendency $\lambda_x \propto z$. For the spanwise direction, only the self-similar tendency is retained. These results are in good agreement with both the Townsend hypothesis of self-similar structures, which states that self-similar eddies scale with wall-normal distance, and that a linear evolution of peak energy production with z/δ should be observed, and with Perret and Patton (2021) above vegetation canopies, where the $\lambda \propto z^2$ is observed.

Well above the canopy, at $z/\delta > 5 \times 10^{-2}$, the scales of the most energetic structures are constant with height, and $\lambda_{x,y} \propto \delta$.

Table 3 summarizes the streamwise and spanwise wavelengths corresponding to the most energetic scales and their tendency with height.

If these spectrograms can not obviously exhibit the presence of inner and outer peaks, as it had been found in high Reynolds number turbulent boundary layers (Mathis et al. 2009) or under weakly convective conditions (Salesky and Anderson 2018), a clear distinction between the evolution of small near-canopy structures and large structures with wall distance is showed in Fig. 7, delimited by the black vertical line. Same result was found in wind-tunnel studies over staggered cubes (Blackman and Perret 2016), and in LES study over vegetation canopies (Perret and Patton 2021). The independence of large structures' wavelengths with wall distance can be interpreted as the signature of the Very Large Scale Motions (VLSMs) in the streamwise velocity field whose streamwise extent scales with δ. Those VLSMs, often reported in the literature (highlighted for high-Reynolds turbulent flows over smooth planes by Hutchins and Marusic 2007, and for near-neutral ABL developing over a rough surface representative of an urban terrain by Inagaki and Kanda 2010), occupy most of the upper part of the boundary layer.

To compare characteristic wavelengths of the present study with litterature, the streamwise wavelengths λ^{max} corresponding to the local maximum of energy extracted from the one-dimensional pre-multiplied auto-spectra $k_x S_x(u,u)$ are reported in Fig. 8, with observations from experimental studies on staggered arrays of cubes using LDA measure-

Table 3 Streamwise and spanwise wavelengths λ_x and λ_y corresponding to the most energetic scales of u in the different regions of the flow for three canopy configurations, normalized by the canopy height h or the ABL depth δ

	$z/\delta < 0.01$	$0.01 < z/\delta < 0.03$		$0.03 < z/\delta < 0.05$		$0.05 < z/\delta$	
	$\lambda_{x,y}/h$	λ_x/δ	λ_y/δ	λ_x/δ	λ_y/δ	λ_x/δ	λ_y/δ
6.25%	≈ 10	$\propto z^2$	$\propto z$	$\propto z$	$\propto z$	2.8	0.7
25%	≈ 10	$\propto z^2$	$\propto z$	$\propto z$	$\propto z$	2.8	0.7
44%	≈ 10	$\propto z^2$	$\propto z$	$\propto z$	$\propto z$	2.8	0.7

ments of Herpin et al. (2018) for the 25% density, hot-wire measurements of Perret et al. (2019) and SPIV data of Basley et al. (2019) for the three canopy densities. This comparison yields remarkably good coherence especially for the densest canopies in the RSL and in the lower region of the log-layer ($(z-d)/\delta < 0.05$). In the upper region of the log-layer ($0.05 < (z-d)/\delta < 0.1$, important differences are noticed for the three densities, but results collapse above the log-layer, where the size of VLSMs remain constant with height at about $\approx 3\delta$.

However, the wavelengths corresponding to the longitudinal VLSMs may be underestimated by this study, since values of $\lambda_x/\delta = 2.8$ are observed, whereas other studies of neutrally stratified, Coriolis-free ABL turbulence (Fang and Porté-Agel 2015; Jacob and Anderson 2017) depict VLSMs streamwise extents that can scale up to $\approx 20\delta$. The influence of the choice of domain dimensions too small for the computation of the largest eddies is seen here. Indeed, the physical domain, of about $(L_x; L_y) = (2.8\delta, 1.4\delta)$ is not long enough to allow for the development of VLSMs. This is why outer peaks are capped at $\lambda_x/\delta = 2.8$. For spanwise spectra, the problem of domain size does not seem to affect the location of outer peaks, since they all scale with sizes lower than the spanwise extent : $\lambda_y/\delta = 5 \times 10^{-1}$ for $\lambda_p = 6.25\%$, 7×10^{-1} for 25% and 1.4 for 44%. It can be important to notice that VLSMs extents obtained for sparse canopies yields similar results as Fang and Porté-Agel (2015) for a neutrally-stratified ABL over a smooth plane ($\lambda_y/\delta = 6 \times 10^{-1}$).

One can notice the emergence of a crest in streamwise spectra with packing density at the canopy top (for $1 \leq z/h \leq 2$). This can be linked with the superposition of small and large scales of turbulent structures inside the canopy and in the RSL observed in Fig. 5. Less dense canopies are mostly affected by the characteristics of LSMs developing in the log-layer but not so by small scale structures. Conversely, canopy and roughness sub-layers of denser canopies are mostly affected by small scales, since there is less penetration of LSMs inside the canopy. This is why a small scale (about $10h$) peak emerges in pre-multiplied spectra of 44%.

In Fig. 9, pre-multiplied two-dimensional auto-spectra of u are considered, in two streamwise-spanwise planes at $z/h = 1.45$ and $z/h = 4.45$ corresponding to the RSL and the log-layer respectively. The capacity to reproduce coherent turbulent structures observed in the literature with the spectral content is first discussed here within the logarithmic

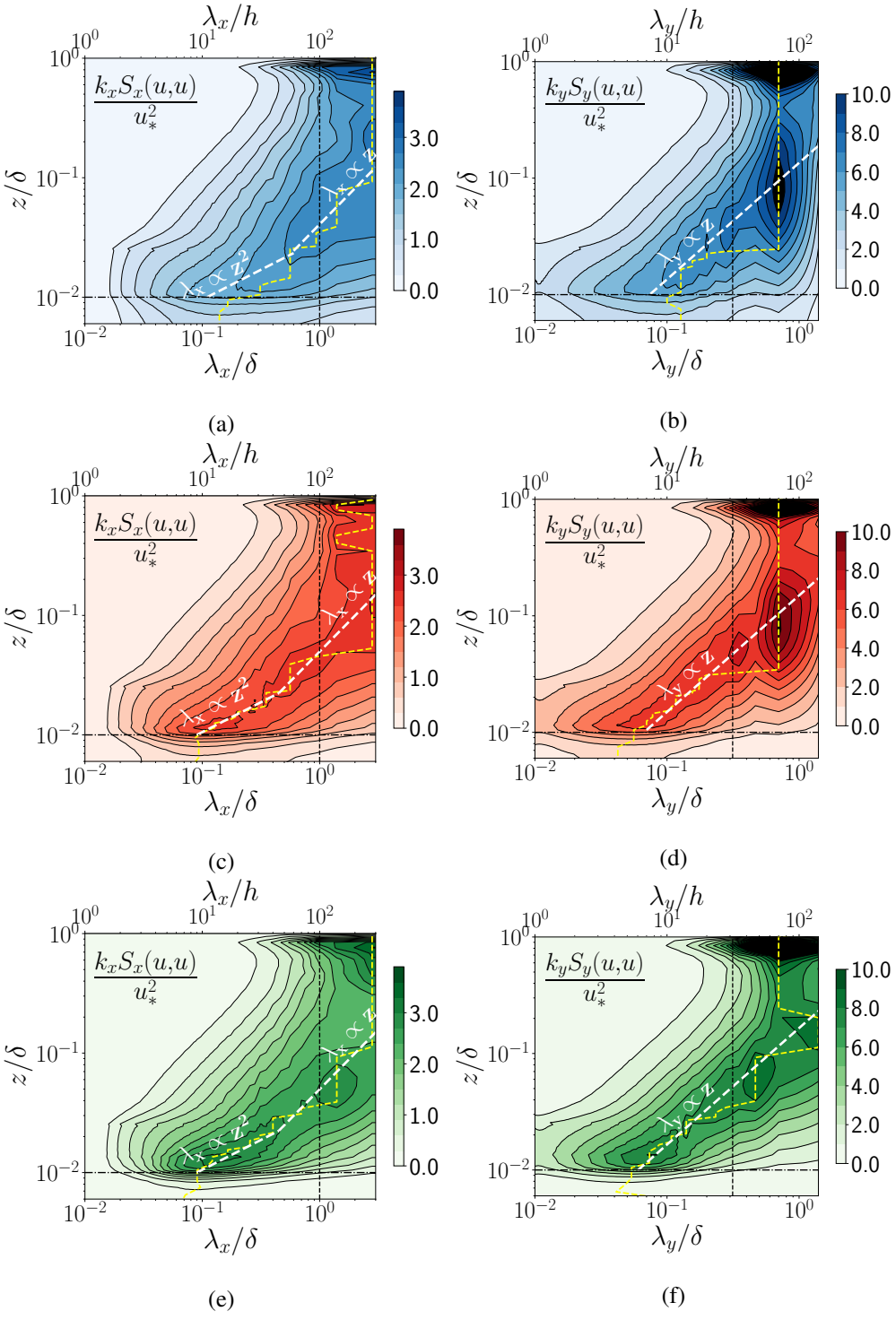

Figure 7 Pre-multiplied spectrograms, plotted as a function of wall-normal distance z/δ, streamwise wavelength λ_x/δ (left) and spanwise wavelength λ_y/δ (right). Pre-multiplied spectra of u normalized by u_*^2 for $\lambda_p = 6.25\%$, $\lambda_p = 25\%$, $\lambda_p = 44\%$ are shown in (a, b), (c, d), and (e, f) respectively. For clarity, spectra are scaled up by a factor of 10^3. The horizontal dash-dotted line corresponds to the canopy top. Oblique dashed white lines corresponds to $\lambda_{x,y} \propto z$ in (a, b, c, d, e, f) and $\lambda_x \propto z^2$ in (a, c, e). The yellow dashed line indicates the location of the local maximum of the spectra, and the vertical black dashed line shows the location of the spectral filter (λ_c/δ)

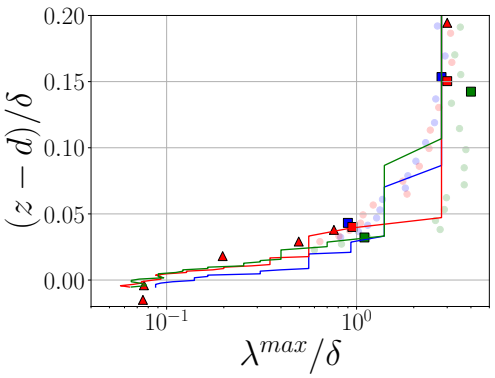

Figure 8 Streamwise wavelengths λ_x^{max} corresponding to the local maximum of energy from the one-dimensional pre-multiplied auto-spectra $k_x S_x(u,u)$ plotted for 6.25, 25 and 44% (blue, red and green solid lines), against wall distance $(z-d)/\delta$. Red triangles are extracted from Herpin et al. (2018), full squares are extracted from the two-dimensional auto-spectra $k_x k_y S(u,u)$ of Basley et al. (2019), and small light circles are extracted from two-dimensional auto-spectra $k_x k_y S(u,u)$ of Perret et al. (2019).

layer at $z/h = 4.45$, hence at the height at which large structures' wavelengths start to become independant with wall distance. The first striking result of the spectral content of the streamwise velocity component in the log-layer is the independence with regards to the packing density. Therefore, each of the following results are valid for the three considered cases. Auto-spectra of u in the log-layer exhibit the presence of a peak of maximum energy centered around $\lambda_x \approx \delta$ and $\lambda_y \approx 0.4\delta$ relative to the spectral signature of LSMs that shows good coherence with the spectrograms of Fig. 7. Analysis of the two-dimensional auto-spectra of u yields the existence of an increasing anisotropy of the structures associated with scales up to $\lambda_x/\delta = 2.8$, since the ridge of maximum energy follows a $\lambda_x \propto \lambda_y^2$ scaling law. The result of this trend is an increasing elongation of low- and high-momentum regions as they get wider. This anisotropic behavior is in agreement with the findings of Basley et al. (2019) and Jiménez et al. (2004) through a study of large-scale dynamics of wall-bounded turbulent flows using DNS. However, at larger scales, Chandran et al. (2017), in their study of high Reynolds number boundary layers over smooth walls, predict that energy crest should depart from the $\lambda_x \propto \lambda_y^2$ scaling law to a self-similar law. Due to the limited streamwise extent of the computational domain, such a trend can not be confirmed here.

Figures 9 (a,c,e) of the pre-multiplied auto-spectra of u within the RSL $(z/h = 1.45)$, show some important differences with characteristics of LSMs developing in the log-layer. The first main difference, in agreement with the spectrograms of Fig. 7, is a shift in spectral content towards smaller scales for the three canopies. The same comment about the anisotropy of large-scale structures $(\lambda_x > 0.2\delta)$, scaling with $\lambda_x \propto \lambda_y^2$ is still valid in the RSL. For smaller structures however, it seems that the ridge of maximum energy is following a self-similar trend, hence leading to the coexistence of both non self-similar and self-similar eddies. This coexistence was first observed by Chandran et al. (2017) in 2D-spectra of experimental and DNS results of low- and high-Reynolds number turbulent wall-bounded flows. For low-Reynolds number flows, the same coexistence is observed (self-similarity of smaller structures, and $\lambda_x \propto \lambda_y^2$ scaling law for larger structures), while the opposite is found at higher Reynolds numbers and in the study

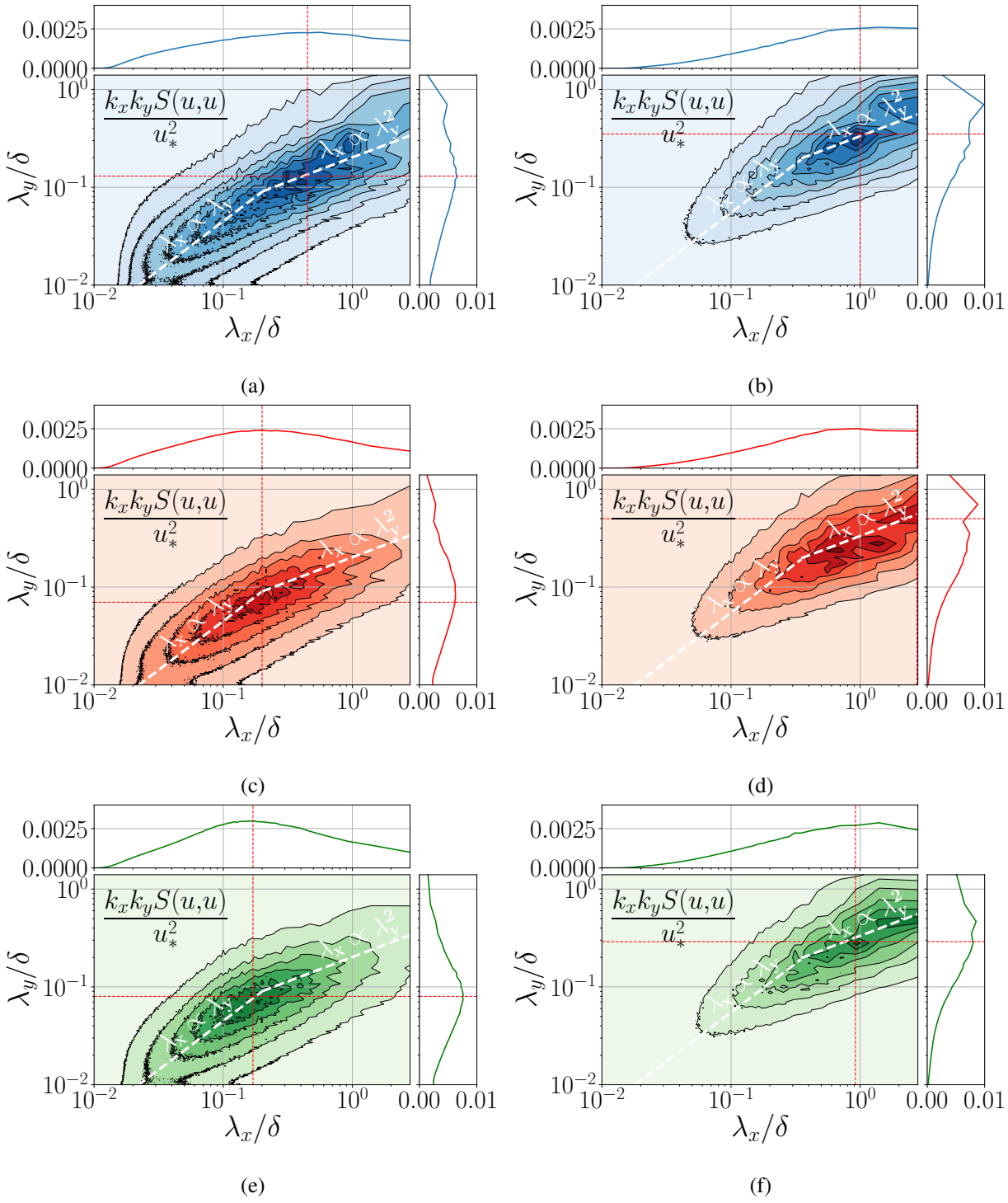

Figure 9 Pre-multiplied auto-spectra in a streamwise-spanwise plane at $z/h = 1.45$ and $z/h = 4.45$ for (a, c, e) and (b, d, f) respectively. Pre-multiplied normalized auto-spectra of u, $k_x k_y S(u,u)/u_*^2$ for $\lambda_p = 6.25\%$, $\lambda_p = 25\%$, $\lambda_p = 44\%$ are shown in (a, b), (c, d), and (e, f) respectively. Oblique dashed white lines corresponds to $\lambda_x \propto \lambda_y$ and $\lambda_x \propto \lambda_y^2$. Red lines intersect at the maximum of the two-dimensional spectra. Contours are shown from 12.5% to 87.5% of the maximum with steps of 12.5%.

of Basley et al. (2019). Due to the high-Reynolds number characteristic of our studied flow ($\delta^+ \approx 2 \times 10^7$), same anisotropic character should be seen here but the limited streamwise extent of the domain prevents from reproducing the self similar trend at larger scales.

Figures 9 (a, c, e) also exhibit a monotonic decrease of maximum energy peak with packing density : an isolated regime would allow strong penetration of LSMs inside the canopy, thus highlighting a strong predominance of LSMs inside the RSL, which manifests in a maximum energy peak occuring at wavelengths close to those observed in the log-layer ($\lambda_x \approx 0.5\delta$, $\lambda_y \approx 0.1\delta$). Conversely, an increasing packing density reduces the impact of LSMs footprints in the RSL and enhances the contribution of canopy-induced turbulent structures, which results in a shift in maximum energy peak towards smaller wavelength ($\lambda_x = 0.2\delta$, $\lambda_y = 0.07\delta$ for $\lambda_p = 25\%$, and $\lambda_x = 0.15\delta$, $\lambda_y = 0.08\delta$ for $\lambda_p = 44\%$). This observation is consistent with the "two-scale" behavior brought forward by Reynolds and Castro (2008) with two-points correlations of the streamwise velocity component near the top of the canopy and which suggest that the large-scale structures existing in the logarithmic layer leave a strong imprint on the flow in the RSL and coexist with structures of similar characteristics and energy yet at smaller scales. Hence, a direct impact of the canopy density on LSMs in the roughness sublayer is seen here, at the opposite of results from the wind tunnel study of Basley et al. (2019) where this superimposition of scales is not brought forward by the 2D-spectra directly, but indirectly through the emergence of an unambiguous secondary, canopy-related, peak in one-dimensional streamwise spectra $k_x S_x(v, v)$.

In order to investigate wall-normal interactions between canopy and RSL, organized mainly in low-velocity upward ejections and high-velocity downward sweeps, auto-spectra of the wall-normal component $k_x k_y S(w, w)/u_*^2$ and co-spectra $-k_x k_y S(u, w)/u_*^2$ (with a negative sign to account for the anti-correlation between u and w) are plotted in a streamwise-spanwise plane $z/h = 1.45$ corresponding to the RSL in Fig. 10.

Auto-spectra of the wall-normal component are characterized by a range of energetic scales of about $0.01\delta - 0.06\delta$, *i.e.* of the order of a few h, in both streamwise and spanwise directions. Larger scales, related to LSMs, have negligible energetic levels. It is observed here that canopy packing density has very small impact on energetic wavelengths of w, contrary to the slight decreasing tendency found in Basley et al. (2019). However, it should be kept in mind that, due to the flatness of peaks in one-dimensional spectra, locating the peak is difficult, and a decreasing wavelength tendency with packing density could be hidden. Nonetheless, this highlights that scales related to wall-normal transport of momentum, and by extension to ejections and sweeps, are associated with canopy interactions, as observed on the basis of field observations for urban canopies in Christen et al. (2007). Additionally, a trend following closely the scaling law $\lambda_x \propto \lambda_y$ that puts in evidence the existence of a self-similarity in the wall-normal component is observed here, and a near isotropic behavior is also depicted in Fig. 10. Same comment can be made on the pre-multiplied co-spectra $-k_x k_y S(u, w)/u_*^2$, whose most energetic structures are scaled in between most energetic scales of w ($\approx 0.03\delta$) and those of u ($\approx 0.1\delta$).

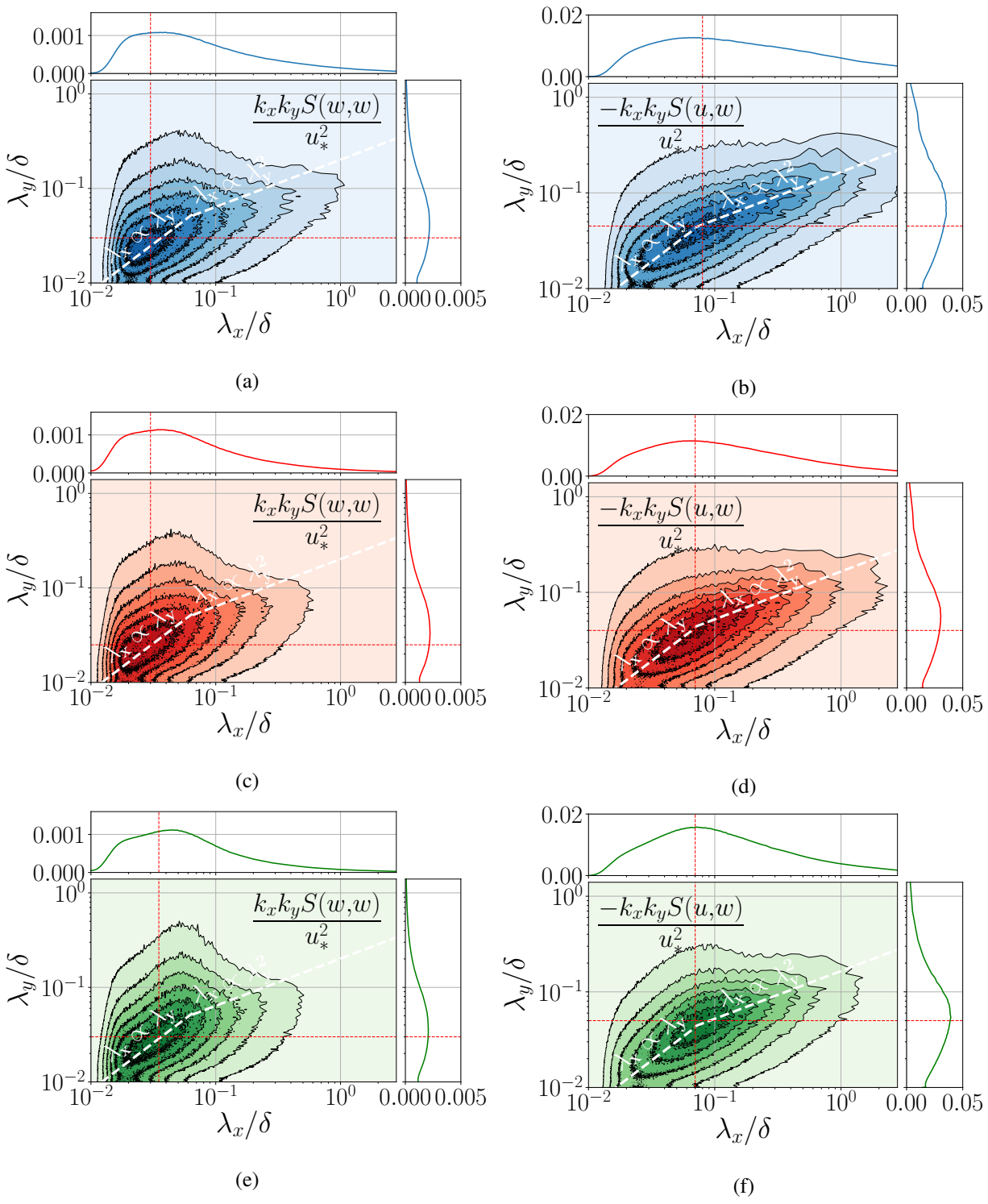

Figure 10 Pre-multiplied auto-spectra of w and pre-multiplied co-spectra of uw in a streamwise-spanwise plane at $z/h = 1.45$ shown in (a, c, e) and (b, d, f) respectively. Pre-multiplied normalized spectra for $\lambda_p = 6.25\%$, $\lambda_p = 25\%$, $\lambda_p = 44\%$ are shown in (a, b), (c, d), and (e, f) respectively. Oblique dashed white lines corresponds to $\lambda_x \propto \lambda_y$ and $\lambda_x \propto \lambda_y^2$. Red lines intersect at the maximum of the two-dimensional spectra. Contours are shown from 12.5% to 87.5% of the maximum with steps of 12.5%.

The spectral analysis presented above reveals that, irrespective of the canopy configuration, upper canopy layers are populated with well-known coherent turbulent structures, presenting a good agreement with the literature. The present logarithmic layers exhibit elongated low- and high-momentum regions corresponding to streaky LSMs, bearing anisotropic and self-similar characters that were found in past studies over wall-bounded flows (Jiménez et al. 2004 and Chandran et al. 2017). A "two-scale" behavior, evidenced by Reynolds and Castro (2008), is particularly visible in the roughness sublayer, where long, streaky LSMs superimpose onto smaller, canopy-induced structures, organized mainly in low-velocity upward ejections and high-velocity downward sweeps, and which appear to scale with a self-similar law close to the canopy. A noticeable impact of the canopy density is observed in the RSL, where an increase in packing density generates more drag and intense shear, leading to a predominance of smaller structures.

3.4. Two-points correlations and inclination angles

In order to complement the spectral analysis performed to identify the turbulent structures developing above a drag-porosity modelled urban canopy and quantify changes in turbulence spatial structure with packing density, the two-point correlation coefficients, their inclination angles and the integral length scales are considered in this section. The one-dimensional two-point correlation coefficients of the streamwise velocity R_{uu} are presented in Fig. 11, and two-dimensional contours of $R_{uu}(dx, z, z_{ref})$ are shown in Fig. 12, where the 2D two-point correlation coefficient of the streamwise velocity is calculated as :

$$R_{uu}(dx, z, z_{ref}) = \frac{\langle u'(x, y, z_{ref}) u'(x + dx, y, z) \rangle}{\sigma_{u(x,y,z_{ref})} \sigma_{u(x+dx,y,z)}} \tag{13}$$

The auto-correlation coefficient $R_{uu}(dx, z, z_{ref})$ in Fig. 11 exhibit a slow decay with the streamwise separation, as an indication of the presence of very long streamwise-elongated structures. The correlation reaches the zero level at $dx/\delta = 1.2$ for all heights within the canopy and the RSL for the sparsest canopy. As for the two denser canopies, the correlation is still around 0.05 inside the RSL at $dx/\delta = 1.4$, and around 0.2 in the log-layer. This increase of the LSMs with canopy density is consistent with the results obtained in Sect. 3.3, and the fact that the largest structures remain correlated with themselves even at the end of the domain highlights conclusion yielded above concerning the limited streamwise extent of the domain, especially for the densest canopy. This is also the reason why negative correlation levels for distances far from the reference point, attributed to the presence of long structures, followed by similar ones but with opposite negative fluctuations are not observed here, as they are in Fang and Porté-Agel (2015). In their study, the dimensions of the computational domain were chosen to be $(L_x, L_y, L_z) = (32\pi L_z, 4\pi L_z, 1000m)$, with a horizontal grid of $\Delta x = \Delta y = 2\pi\Delta z$, resulting in cells approximately 20 times larger than the cells studied here, for relatively similar number of cells. However, Fang and Porté-Agel (2015) performed their LES study over a smooth plane in order to investigate VLSMs at high Reynolds number : such an approach is not feasible nor wanted in our case, since the objective is to study the influence of wall roughness on dynamics and interaction of coherent structures in the lowest layers of the ABL.

The changes with packing density of typical scales estimated from the correlation that occur inside and at the canopy

top can be noticed in Fig. 11. Sparse canopies are populated with relatively long elongated structures, and correlation lengths present few changes with increasing wall distance. This is a sign of a "one-scale" behavior, where the imprint of LSMs remains strong inside the canopy due to isolated obstacles (or in our case, small drag forcing). On the other hand, correlation lengths are largely reduced for denser canopies, with a streamwise correlation length of about $dx/\delta = 0.1$ inside the canopy for $\lambda_p = 44\%$. This is a sign of a "two-scale" behavior, that results in a decoupling between flows in the canopy or near-canopy region, and above (*i.e.* in the log-layer).

In the spanwise direction, the correlations show an alternating positive-negative trend which is a sign of alternating low- and high- momentum regions, visible in instantaneous fields in Fig. 5. The scale corresponding to the location of the first zero-crossing of the correlation coefficient of the streamwise velocity and its evolution with packing density ($dy/\delta \approx 0.18$ for 6.25%, ≈ 0.3 for 25% and ≈ 0.4 for 44%) shows an increase in spanwise width of the streaks with density ($\approx 0.32\delta$ for 6.25%, $\approx 0.4\delta$ for 25% and $\approx 0.7\delta$ for 44%). Overall, the characteristic spanwise width found here shows good match with results obtained from LES of wall-bounded flows of Fang and Porté-Agel (2015). An interesting result is the height at which the alternating positive-negative trend occur for each configuration. Indeed, if this alternating trend is systematically present in the log-layer for all densities, it appears that the only correlation function inside the canopy and in the RSL that follows the trend is the one for the sparsest density case. This echoes the snapshots taken at $z/h = 1.45$ in Fig. 5, where a large-scale organization develops in the RSL for the sparsest density, in which the alternation of low- and high-momentum streaks is seen.
The auto-correlation functions of the vertical velocity component R_{ww} (not shown here) yield similar results as in Sect. 3.3 : a streamwise extension of correlated regions of about 0.1δ, a spanwise extension of few h, and the absence of a clear trend concerning the evolution of correlated structure' sizes with density.

Additional information concerning the shape of coherent structures developing in the RSL and in the log-layer is given by two-point correlation maps in Fig. 12. As previously observed in wind tunnel and LES (Maché 2012) simulations, $R_{uu}(dx, z, z_{ref})$ yields a near-elliptical form in the $x - z$ plane, with a downwind tilt from the horizontal. This downwind tilt is estimated using the $R_{uu}(dx, z, z_{ref}) = 0.4$ iso-contour (highlighted with white iso-contours in Fig. 12), commonly used to approach the calculation of the integral length scale. The inclination angles of $R_{uu}(dx, z, z_{ref})$, that have been computed for all canopies with the same procedure, are presented in Table 4. An increase in the inclination angle with density is observed, probably due to the larger wind shear above the canopy, which enables the inclination of coherent structures. Similar results were observed with the same atmospheric LES solver over vegetation canopies of various densities by Dupont and Brunet (2008b), in wind-tunnel measurements over cubes (Reynolds and Castro 2008), and with DNS over resolved cubic obstacles (Coceal et al. 2006).

The 0.4 iso-contour shown in Fig. 12 gives clue about the characteristic length scales of coherent eddies, but Fig. 13 showing the wall-normal evolution of the integral length scale (calculated using the 0.4 criterion) is used for further discussion. In Fig. 13, integral length scale of the streamwise velocity component are presented in the

Table 4 Inclination angles (°) of the spatial 2D two-point correlation function for the streamwise velocity $R_{uu}(dx, z, z_{ref})$

z_{ref}/h	λ_p = 6.25%	λ_p = 25%	λ_p = 44%
1.45	10.82	16.24	17.05
4.45	9.77	12.00	11.87

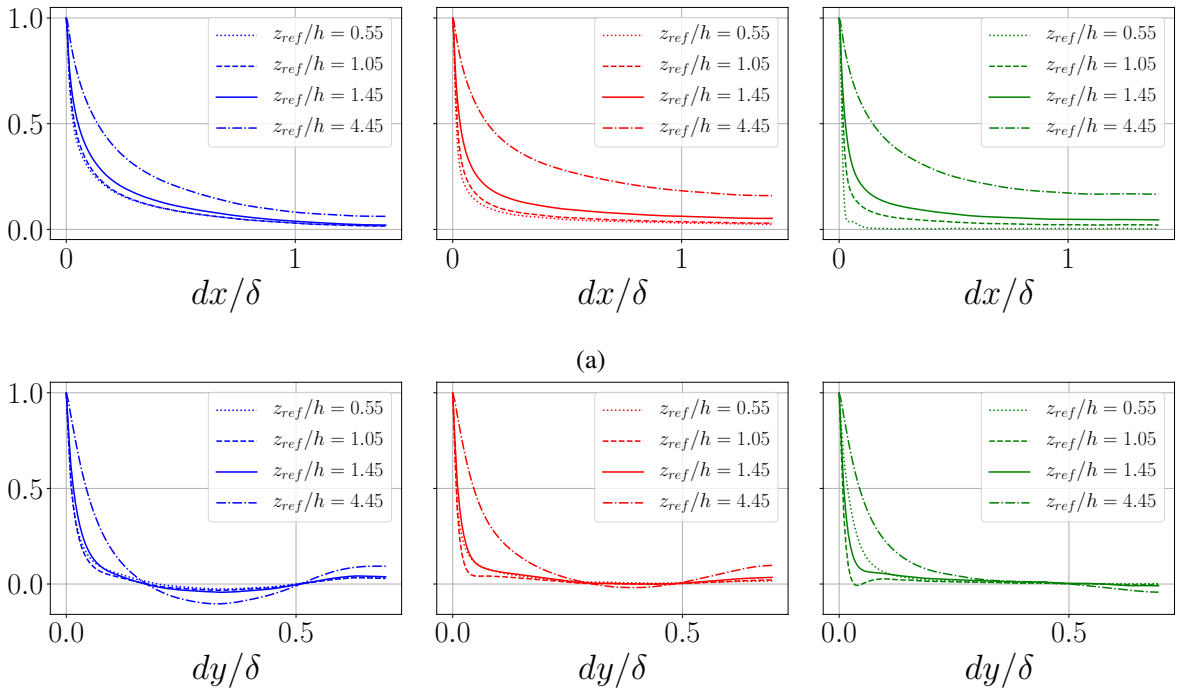

Figure 11 Horizontal variation of the spatial correlation coefficient of the streamwise velocity R_{uu} in the longitudinal (*a*) and spanwise (*b*) directions. The correlation coefficients are evaluated for λ_p = 6.25% (left), 25% (center) and 44% (right).

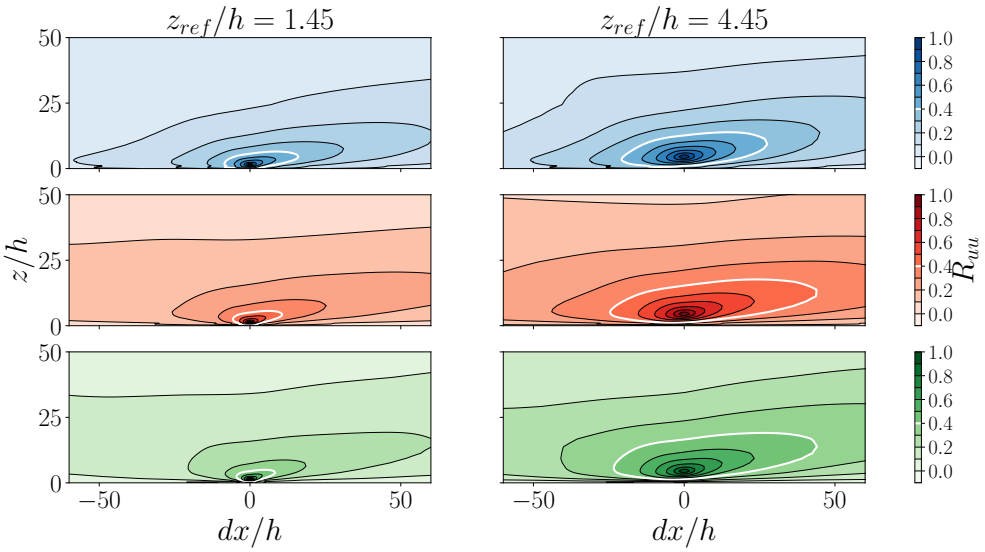

Figure 12 Two-point correlation maps of $R_{uu}(dx, z, z_{ref})$, plotted as a function of streamwise (dx/h) and vertical (dz/h) separations, for $\lambda_p = 6.25\%$ (top), 25% (middle) and 44% (bottom). Panels are plotted in the RSL (at $z_{ref}/h = 1.45$, left) and in the log-layer ($z_{ref}/h = 4.45$, right). Iso-levels are shown from 0 to 1 with increments of 0.1. White iso-contours show the $R_{uu} = 0.4$ iso-level.

streamwise (Λ_{u_x}), the spanwise (Λ_{u_y}), vertical positive ($\Lambda_{u_{z+}}$) and vertical negative ($\Lambda_{u_{z-}}$) directions. A relatively constant evolution of integral length scale with height inside the canopy for the two densest canopies of $\Lambda_u \approx 3h$ is observed at canopy top, and $\approx 5h$ for $\lambda_p = 6.25\%$, which is consistent with Castro et al. (2006) results. As reported in the literature, Λ_{u_y}, $\Lambda_{u_{z+}}$ and $\Lambda_{u_{z-}}$ stay relatively constant inside the canopy, and $\Lambda_{u_y} = \Lambda_{u_z} \approx h$ at canopy top. Above the canopy, for $1 < z/h < 5$ (*i.e.* in the RSL and bottom part of log-layer) a linear increase of integral length scale of u in the $x-$direction is observed for all three canopies, with different slopes (steeper as the canopy gets sparser). Above $z/h = 5$, Λ_{u_x} largely decreases and differences in levels reached in log-layer are observed from one density to another : about $30h$ for 6.25%, $45h$ for 25%. The wall-normal evolution is different for the densest canopy, as the streamwise integral length reaches very high levels (above $60h$ at $z/h = 20$) and does not reach a steady value : this is a consequence of the limited extent of the computational domain, too small to represent the largest scales in this case.

Vertical profiles of integral length scale in the positive and negative vertical direction are displayed in Fig. 13 to assess the distance from the roughness at which the attached eddies detached from the wall (distance above which the slopes of the profiles of $\Lambda_{u_{z-}}$ and $\Lambda_{u_{z+}}$ would coincide). It appears that this feature is observed for the three packing densities above $z/h = 10$. Hence, these further detached VLSMs (referred as type-C eddies in Perry and Marušić 1995) which contribute to the high-wavenumber motions with length scales not directly related to their distance to the canopy start developing at $z/h = 10$.

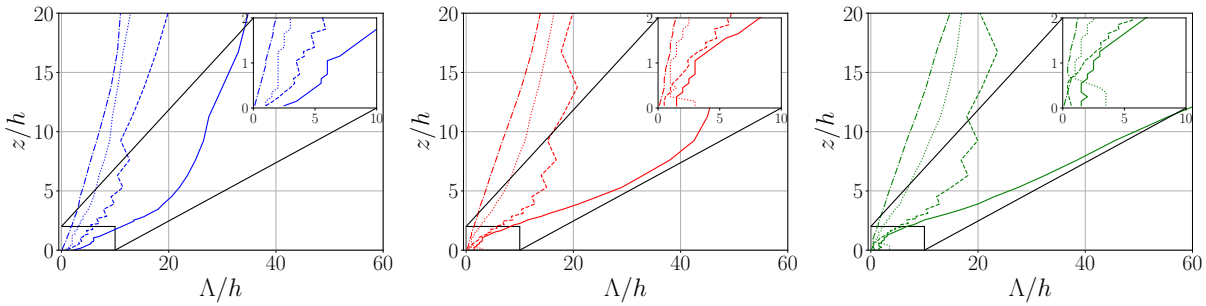

Figure 13 Wall-normal profiles of integral length scales of the streamwise velocity in the streamwise, spanwise, positive vertical and negative vertical directions for $\lambda_p = 6.25\%$ (*a*), 25% (*b*) and 44% (*c*). Solid lines denote Λ_{u_x}/h, dotted lines are Λ_{u_y}/h, dashed lines $\Lambda_{u_{z+}}/h$ and dashed-dotted lines $\Lambda_{u_{z-}}/h$.

3.5. Interaction between the most energetic scales

Recent studies of high-Reynolds wall-bounded flows have evidenced the existence of an interaction mechanism that resembles an amplitude modulation process of the most energetic near-wall scales by the most energetic scales present in the outer region (see Mathis et al. 2009; Blackman and Perret 2016; Salesky and Anderson 2018; Blackman et al. 2019 among others). The capacity of the drag-porosity model to reproduce this key feature, which suggest that the near-wall turbulence is triggered by the largest scales of the flow through a phase relationships, is presented here. The spectral analysis presented in the previous sections clearly showed the distinct signature of both the near-canopy turbulence and that related to ABL-scales through the presence of two clear peaks in the spectra. Therefore, following Mathis et al. (2009), the scale separation is performed here via the use of a low-pass filter to extract from the velocity field the large-scale component u_L associated with the largest energetic scales and decompose, for instance, the instantaneous streamwise velocity u into a space-time averaged mean $\langle u \rangle$, large-scale fluctuations u'_L and small-scale fluctuations u'_S :

$$u = \langle u \rangle + u'_L + u'_S \tag{14}$$

The cut-off wavelength of the low-pass filter is determined using the pre-multiplied spectrograms of streamwise velocity presented above in Fig. 7, and is chosen so as to separate the most energetic scales present above the logarithmic layer and those in the near-canopy region. The dotted black lines in Fig. 7 show the location of the cut-off, chosen to be $\lambda_c = \delta$ for packing densities of $\lambda_p = 6.25\%$ and 25%, and $\lambda_c = 2\delta$ for 44%, which results in the same cut-off wavelength as in Blackman and Perret (2016) in their experimental results over a staggered cube canopy of $\lambda_p = 25\%$. Basley et al. (2018) showed that the choice of the cut-off wavelength is not a critical point as long as it is located between the inner and outer spectral peaks. Following this result, no further investigation on the location of the spectral filter has been addressed here. Mathis et al. (2009) originally proposed using the correlation coefficient between the large scale component u'_L and the low-pass filtered envelope of the small scales u'_S, the so-called amplitude modulation coefficient, as an indicator of the existence and the importance of the amplitude modulation mechanism. They

later showed that the cross-correlation $\langle u'_L u'^2_S \rangle$, resulting from the scale-decomposition of the third-order moment $\langle u'^3 \rangle = \langle u'^3_L \rangle + 3\langle u'_L u'^2_S \rangle + \langle u'^2_L u'_S \rangle + \langle u'^3_S \rangle$ was directly related to the degree of amplitude modulation (Mathis et al. 2011). This latter approach is employed here to quantify the amplitude modulation of the (small) near-canopy scales by the (large) ABL scales. The investigation is extended to the three velocity components using the same filtering method.

The contributions of large- and small-scales to the averaged Reynolds stress components have been investigated (not shown here) in order to compare their relative contribution to the total Reynold stresses with the literature results. Within the roughness sublayer and in the canopy, u'_S contributes to the majority of the variances and shear stresses, approximately 85%, 95% and 90% to $\langle u'u' \rangle$, $\langle w'w' \rangle$ and $\langle u'w' \rangle$, respectively, for the three configurations at $z/h = 1.45$. As a comparison, similar results were obtained by Inagaki and Kanda (2010) and Blackman et al. (2019) (60%, 90% and 90% respectively). Above the RSL (in the log-layer), the contribution of the large-scale component overtakes that of small-scales from $z/h = 3$ for $\lambda_p = 6.25\%$ and 25%, and $z/h = 4$ for 44%, for the variance of u and the shear stress. Regarding the variance of w, the small-scale contribution is consistently more important than the large-scales, over the whole RSL and log-layer extent. Overall, no clear trend with λ_p have been observed.

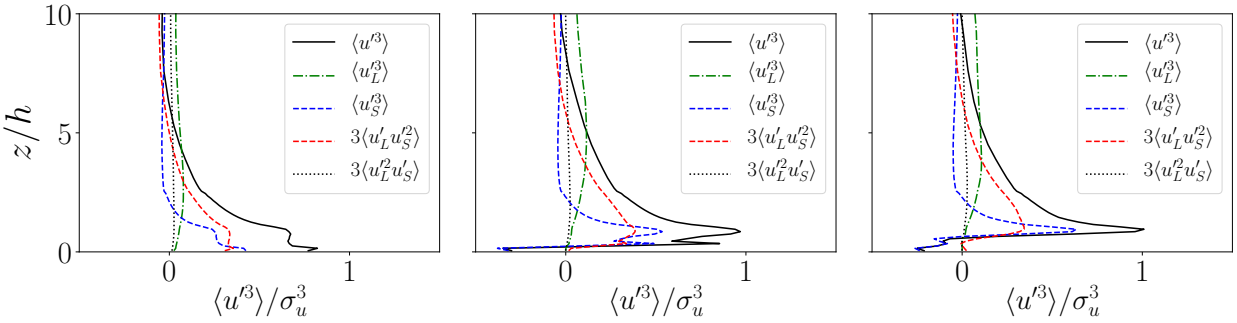

Figure 14 Skewness decomposition of the streamwise velocity $\langle u'^3 \rangle$ in small-scale skewness $\langle u'^3_S \rangle$, large-scale skewness $\langle u'^3_L \rangle$, and cross-terms $3\langle u'_L u'^2_S \rangle$ and $3\langle u'^2_L u'_S \rangle$, for canopy density 6.25% (left), 25% (center) and 44% (right). All components are spatially and temporally averaged, and normalized by σ_u^3.

Figure 14 shows the scale-decomposed skewness factor of the streamwise velocity. It appears that, for all canopy configurations, the decomposed skewness exhibits a peak at the canopy top ($z/h = 1$) that is most largely due to the combined contribution of the small-scale component $\langle u'^3_S \rangle$ and the cross-term $\langle u'_L u'^2_S \rangle$. The combination of this strongly positive u_S skewness and strongly negative w skewness (shown in Fig. 3) indicates that the predominance of intermittent downward moving gusts (sweeps) is mainly influenced by small-scales. Both quantities become negative above, at $z/h \approx 2$ for $\langle u'^3_S \rangle$ and above $6h$ for the cross-term, thus showing similarities with the skewness profile of a mixing layer, which agrees with Perret and Kerhervé (2019) and Blackman et al. (2019). The asymmetric character of the flow shows relatively high dependence on the packing density : denser canopies produce stronger shear at the canopy top resulting in higher skewness values. Alternatively, the large-scale component and the cross-term $\langle u'^2_L u_S \rangle$

contribute a negligible amount to the skewness in the RSL, and a non-negligible contribution of $\langle u_L'^3 \rangle$ is observed only in the log-layer. The cross-term $\langle u_L' u_S'^2 \rangle$ represent the non-linear effect of large-scale motions onto smaller scales : its non-negligible wall-normal profile could suggest a mechanism such as amplitude modulation, as suggested by Mathis et al. (2011).

The cross term in the skewness decomposition responsible for the interaction between large- and small-scales and its influence on all three velocity components is further investigated in Fig. 15. In particular, the non-linear interaction between the large-scale momentum motions and the spanwise ($\langle u_L' v'^2 \rangle$) and the vertical ($\langle u_L' w'^2 \rangle$) non-filtered velocity components is compared with $\langle u_L' u_S'^2 \rangle$. Similarly as in the literature (Perret and Kerhervé 2019; Blackman and Perret 2016), the interaction between large-scales and small-scales in the RSL occurs in a similar manner for all flow components.

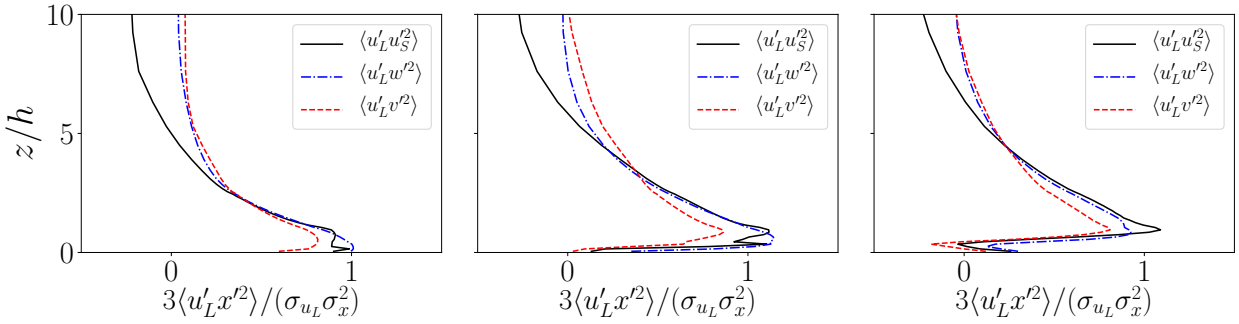

Figure 15 Cross-terms of the skewness decomposition,$\langle u_L' u_S'^2 \rangle$ (black line), $\langle u_L' v'^2 \rangle$ (red dashed line) and $\langle u_L' w'^2 \rangle$ (blue dashed-dotted line). All components are spatially and temporally averaged, and normalized by $\sigma_{u_L} \sigma_x^2$

4. Conclusions

The simulations of the atmospheric boundary layer developing over urban canopies modelled using a drag-porosity approach and a drag coefficient varying with height served as a basis to assess the capacity of such a rough-wall model to reproduce the key features of the spatio-temporal organization of these high Reynolds number flows. Detailed comparisons with the literature of various quantities ranging from the standard one-point statistics to the investigation of the existence of the amplitude modulation mechanism of the near-canopy turbulence by the largest scales showed the very good performance of the proposed approach to reproduce the characteristics of the urban flows in the well-known three typical flow regimes (Grimmond and Oke 1999).

The presence of LSMs and VLSMs was observed qualitatively through snapshots, and quantitatively with spectral analysis, which revealed that, irrespective of the canopy configuration, upper canopy layers are populated with elongated low- and high-momentum regions corresponding to streaky LSMs, bearing anisotropic and self-similar characters that were also found in studies over smooth wall-bounded flows (Jiménez et al. 2004 and Chandran et al.

2017). Further detached meandering VLSMs were identified above $z/h = 10$ and occupy most of the upper part of the boundary layer. The wavelengths of these streaky VLSMs were found to be independent of wall distance and canopy density, and to scale up to 2.8δ, with a spanwise width of about $\approx 0.7\delta$.

The "two-scale" behavior introduced by Reynolds and Castro (2008), was also observed in snapshots with broke-up streaks in the near-wall region, and in two-dimensional spectra. Indeed, long, streaky LSMs superimpose with smaller, canopy-induced structures, organized mainly in low-velocity upward ejections and high-velocity downward sweeps, and which appeared to follow a self-similar evolution with the wall-normal distance close to the canopy, thus reminiscent of the Townsend (1976) and Perry and Marušić (1995) hypothesis of wall-attached self-similar eddies.

A noticeable impact of the canopy density was highlighted in the RSL, where an increase in packing density generates more mean shear, and leads to a predominance of smaller structures, which was observed particularly in two-dimensional spectra of u. Hence, the scales related to ejections and sweeps, responsible for a major part of wall-normal transport of momentum were proven to show dependence on the canopy pattern, as in Christen et al. (2007). Additionally, the two-point correlations yielded an important contrast between sparse canopies, where a "one-scale" behavior occurs, and dense canopies where a decoupling of the flow between the near-canopy and upper regions is observed.

Further investigation was performed to identify the interaction mechanisms that governs flow dynamics within the RSL. Based on a wavelength spectral filtering method separating the most energetic structures of the ABL from those generated in the near-canopy region, as suggested by Mathis et al. (2009), a triple decomposition of skewness showed the major contribution of the small-scale to this quantity in the RSL, and thus to the flow dynamics. This analysis also objectively confirmed the existence of a non-linear interaction mechanism resembling an amplitude modulation mechanism of the small scales by the larger scales, that has been qualitatively observed in instantaneous snapshots of the velocity field, as in previous studies in similar canopy configurations (Blackman and Perret 2016; Basley et al. 2018; Blackman et al. 2019).

Overall, this work assesses the good agreement of the model with the literature : the key features of rough-wall flows are correctly reproduced and the model shows consistent tendency when varying the packing density. The validity of this approach brings forward the important result, also noted in Varghese and Durbin (2020), that drag alone is essential for the computation of unsteady near-wall processes within and above the RSL. Hence, the developed approach could be an essential asset to properly characterize the turbulent flow for wind loading studies on high-rise building in the urban environment, wich remains a challenge despite research efforts on the inflow generation methods for large eddy simulation (Thordal et al. 2019). Whilst this model helps to reduce the number of computational cells, thereby saving some computational costs, a number of important flow characteristics cannot be reproduced, especially

within the canopy, such as recirculating regions due to the absence of obstacles, which is why results obtained in this layer were not analysed in detail in this work. However, this approach has proven to be a powerful tool which, when coupled with more detailed neighbourhood scale simulations, should provide access to the multi-scale interactions between the urban boundary layer flow and the flow within the canopy.

Acknowledgements

This work was granted access to the HPC resources of CINES under the allocation 2020-A0080100132, 2021-A0100100132 and 2022-A0120100132 made by GENCI.

Data availability statement

The data that support the findings of this study are available from the corresponding author, Q. Bucquet, upon reasonable request.

Conflict-of-interest statement

All authors certify that they have no affiliations with or involvement in any organization or entity with any financial interest or non-financial interest in the subject matter or materials discussed in this manuscript.

A. Grid convergence study

In order to investigate the effects of grid resolution on results from our LES, we performed several additional simulations of the $\lambda_p = 25\%$ case on a $280h \times 140h \times 140h$ m^3 domain with 4 different horizontal grid resolutions, ranging from $\Delta x = \Delta y =$ 2m to 20m. The simulations were configured as described in Sect. 2.3, where $u_g = 12$ m.s^{-1}. Simulations were run for approximately 700 canopy-based turnover times $\tau_r = h/u_*$ for simulations A and B, while simulations C and D where initialized with converged fields from coarser resolutions (simulations B and C respectively), and then run for $350\tau_r$ and $150\tau_r$ respectively. Simulation D was not further pursued until $350\tau_r$ mainly for calculation costs, and because the statistical steady-state was already reached, according to a time convergence study not presented here. Averages were calculated over the last $140\tau_r$ s computed. Parameters of the simulations for the grid convergence tests can be found in Table A.5.

Wall-normal profiles of the main statistics from each grid resolution can be found in Fig. A.1, where the mean streamwise velocity profile is displayed with the standard deviation of u , v and w, and their skewnesses. Standard deviation of w and skewnesses are relatively insensitive to the grid refinement, except within the canopy region. Mean streamwise vertical profile appear sensitive to grid resolution, but a grid-resolution independence seems to be reached for this first-order moment in simulations B, C and D. Profiles of the standard deviation of the streamwise and spanwise

Table A.5 Properties of simulations for grid convergence study

Simulation	Cells number	$\Delta x = \Delta y$	Δt	u_*	z_0/h	d/h
-	-	m	s	m s^{-1}	-	-
A	(140, 70, 59)	20	0.05	0.368	0.056	0.978
B	(280, 140, 59)	10	0.05	0.381	0.097	0.935
C	(560, 280, 59)	5	0.05	0.346	0.119	0.695
D	(1400, 700, 59)	2	0.03	0.309	0.146	0.549

components σ_u and σ_v show the largest variations with grid refinement, grid independence seems to be reached only for the two finest grids, in simulations C and D. A resolution of $560 \times 280 \times 59$ (corresponding to simulation C) is sufficient to make one-point statistics insensitive to grid refinement. The grid sensitivity of auto-spectra of the streamwise velocity component is shown in Fig. A.2. Both simulations A and B are proven to be inadequate in computing the energy-producing large scales and the energy cascade following the $-5/3$ law. Conversely, simulations C and D show the presence of an inertial range in the spectra and show good agreement with each other in their overlapping wavelength range. Comparison between simulations C and D shows the clear spectral cut-off effect of the grid, which is observed for simulation C at scales smaller than $1.5h$.

This grid-sensitivity analysis showed the best compromise between the computational cost and grid independence of the statistical characteristics of the simulated flows is obtained with the numerical set-up of simulation C with a horizontal resolution of $\Delta x = \Delta y = 5$ m ($= h/2$).

References

Awol, A., Bitsuamlak, G., Tariku, F., 2022. A new analytical model for wind flow in canopies. Journal of Wind Engineering and Industrial Aerodynamics 225, 105003.

Bannister, E. J., Cai, X., Zhong, J., MacKenzie, A. R., 2021. Neighbourhood-Scale Flow Regimes and Pollution Transport in Cities. Boundary-Layer Meteorol 179 (2), 259–289.

Basley, J., Perret, L., Mathis, R., 2018. Spatial modulations of kinetic energy in the roughness sublayer. Journal of Fluid Mechanics 850, 584–610.

Basley, J., Perret, L., Mathis, R., 2019. Structure of high Reynolds number boundary layers over cube canopies. Journal of Fluid Mechanics 870, 460–491.

Blackman, K., Perret, L., 2016. Non-linear interactions in a boundary layer developing over an array of cubes using stochastic estimation. Physics of Fluids 28 (9), 095108.

Blackman, K., Perret, L., Mathis, R., 2019. Assessment of inner–outer interactions in the urban boundary layer using a predictive model. Journal of Fluid Mechanics 875, 44–70.

Blocken, B., 2014. 50 years of Computational Wind Engineering: Past, present and future. Journal of Wind Engineering and Industrial Aerodynamics 129, 69–102.

Busse, A., Sandham, N. D., 2012. Parametric forcing approach to rough-wall turbulent channel flow. Journal of Fluid Mechanics 712, 169–202.

Castro, I. P., 2017. Are Urban-Canopy Velocity Profiles Exponential? Boundary-Layer Meteorol 164 (3), 337–351.

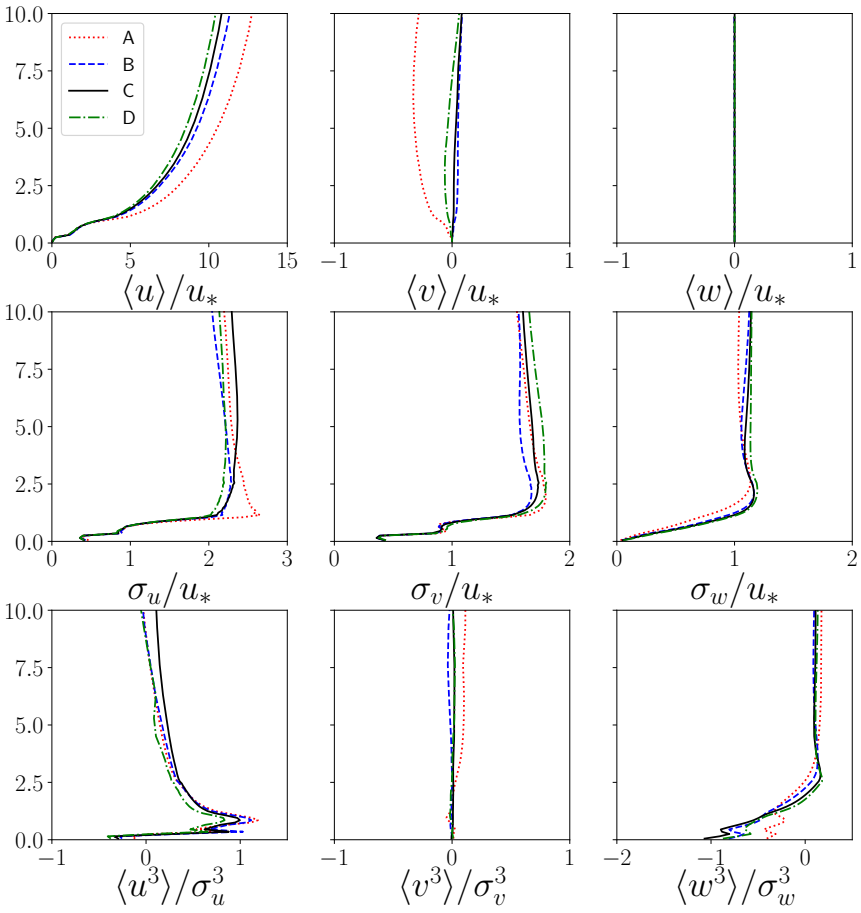

Figure A.1 Convergence of the vertical profiles of the main one-point statistics with grid resolution.

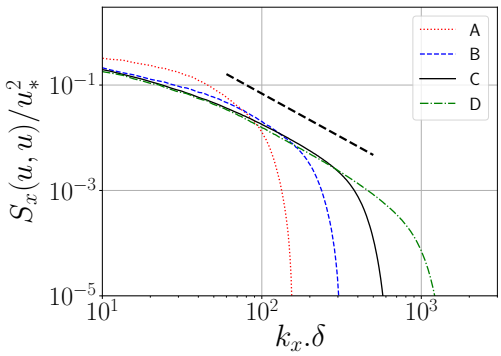

Figure A.2 Convergence of auto-spectra of u in the x-direction at $z/h = 1.45$ with grid resolution. The black dashed line depicts the $-5/3$ law.

Castro, I. P., Cheng, H., Reynolds, R., 2006. Turbulence Over Urban-type Roughness: Deductions from Wind-tunnel Measurements. Boundary-Layer Meteorology 118 (1), 109–131.

Chandran, D., Baidya, R., Monty, J. P., Marusic, I., 2017. Two-dimensional energy spectra in high-Reynolds-number turbulent boundary layers. Journal of Fluid Mechanics 826.

Cheng, H., Hayden, P., Robins, A. G., Castro, I. P., 2007. Flow over cube arrays of different packing densities. Journal of Wind Engineering and Industrial Aerodynamics 95 (8), 715–740.

Cheng, W.-C., Porté-Agel, F., 2016. Large-eddy simulation of flow and scalar dispersion in rural-to-urban transition regions. International Journal of Heat and Fluid Flow 60, 47–60.

Christen, A., van Gorsel, E., Vogt, R., 2007. Coherent structures in urban roughness sublayer turbulence. International Journal of Climatology 27, 1955–1968.

Coceal, O., Belcher, S. E., 2004. A canopy model of mean winds through urban areas. Quarterly Journal of the Royal Meteorological Society 130 (599), 1349–1372.

Coceal, O., Dobre, A., Thomas, T. G., Belcher, S. E., 2007. Structure of turbulent flow over regular arrays of cubical roughness. Journal of Fluid Mechanics 589, 375–409.

Coceal, O., Thomas, T. G., Castro, I. P., Belcher, S. E., 2006. Mean Flow and Turbulence Statistics Over Groups of Urban-like Cubical Obstacles. Boundary-Layer Meteorology 121 (3), 491–519.

Dupont, S., Brunet, Y., 2008a. Edge Flow and Canopy Structure: A Large-Eddy Simulation Study. Boundary-Layer Meteorol 126 (1), 51–71.

Dupont, S., Brunet, Y., 2008b. Influence of foliar density profile on canopy flow: A large-eddy simulation study. Agricultural and Forest Meteorology 148 (6), 976–990.

Fang, J., Porté-Agel, F., 2015. Large-Eddy Simulation of Very-Large-Scale Motions in the Neutrally Stratified Atmospheric Boundary Layer. Boundary-Layer Meteorology 155.

Finnigan, J. J., Shaw, R. H., 2008. Double-averaging methodology and its application to turbulent flow in and above vegetation canopies. Acta Geophysica 56 (3), 534–561.

Giometto, M. G., Christen, A., Meneveau, C., Fang, J., Krafczyk, M., Parlange, M. B., 2016. Spatial Characteristics of Roughness Sublayer Mean Flow and Turbulence Over a Realistic Urban Surface. Boundary-Layer Meteorol 160 (3), 425–452.

Grimmond, C. S. B., Oke, T. R., 1999. Aerodynamic Properties of Urban Areas Derived from Analysis of Surface Form. Journal of Applied Meteorology and Climatology 38 (9), 1262–1292.

Herpin, S., Perret, L., Mathis, R., Tanguy, C., Lasserre, J.-J., 2018. Investigation of the flow inside an urban canopy immersed into an atmospheric boundary layer using laser Doppler anemometry. Experiments in Fluids 59.

Hiraoka, H., 1993. Modelling of turbulent flows within plant/urban canopies. Journal of Wind Engineering and Industrial Aerodynamics 46-47, 173–182.

Hutchins, N., Marusic, I., 2007. Evidence of very long meandering features in the logarithmic region of turbulent boundary layers. Journal of Fluid Mechanics 579, 1–28.

Inagaki, A., Kanda, M., 2010. Organized Structure of Active Turbulence Over an Array of Cubes within the Logarithmic Layer of Atmospheric Flow. Boundary-Layer Meteorology 135, 209–228.

Ismail, U., Zaki, T. A., Durbin, P. A., 2018. The effect of cube-roughened walls on the response of rough-to-smooth (RTS) turbulent channel flows. International Journal of Heat and Fluid Flow C (72), 174–185.

Jackson, P. S., 1981. On the displacement height in the logarithmic velocity profile. Journal of Fluid Mechanics 111, 15–25, publisher: Cambridge University Press.

Jacob, C., Anderson, W., 2017. Conditionally Averaged Large-Scale Motions in the Neutral Atmospheric Boundary Layer: Insights for Aeolian Processes. Boundary-Layer Meteorology 162.

Jiménez, J., Álamo, J. C. D., Flores, O., 2004. The large-scale dynamics of near-wall turbulence. Journal of Fluid Mechanics 505, 179–199.

Kanda, M., 2006. Large-Eddy Simulations on the Effects of Surface Geometry of Building Arrays on Turbulent Organized Structures. Boundary-

Layer Meteorology 118 (1), 151–168.

Kono, T., Tamura, T., Ashie, Y., 2010. Numerical Investigations of Mean Winds Within Canopies of Regularly Arrayed Cubical Buildings Under Neutral Stability Conditions. Boundary-Layer Meteorology 134, 131–155.

Leonardi, S., Castro, I. P., 2010. Channel flow over large cube roughness: a direct numerical simulation study. Journal of Fluid Mechanics 651, 519–539.

Li, C., Wang, J., Hu, G., Li, L., Xiao, Y., 2020. RANS simulation of horizontal homogeneous atmospheric boundary layer over rough terrains by an enriched canopy drag model. Journal of Wind Engineering and Industrial Aerodynamics 206, 104281.

Liu, Z., Ishihara, T., He, X., Niu, H., 2016. LES study on the turbulent flow fields over complex terrain covered by vegetation canopy. Journal of Wind Engineering and Industrial Aerodynamics 155, 60–73.

Macdonald, R. W., Carter, S., Slawson, P., 2000. Measurements of mean velocity and turbulence statistics in simple obstacle arrays at 1:200 scale. Tech. rep., University of Waterloo.

Macdonald, R. W., Griffiths, R. F., Hall, D. J., 1998. An improved method for the estimation of surface roughness of obstacle arrays. Atmospheric Environment 32 (11), 1857–1864.

Maché, M., 2012. Représentation multi-échelles des transferts entre couche de canopée urbaine et atmosphère à l'échelle de la ville. Ph.D. thesis, Bretagne Loire, Nantes.

Maché, M., Calmet, I., Sini, J.-F., 2010. Analysis of the dynamical interactions between atmosphere and urban canopies of different densities using a drag force approach. In: Proceedings of 2010 13th Conference on Harmonisation within Atmospheric Dispersion Modelling for Regulatory Purposes. Paris, France, pp. 668–672.

Martilli, A., Clappier, A., Rotach, M. W., 2002. An Urban Surface Exchange Parameterisation for Mesoscale Models. Boundary-Layer Meteorology 104 (2), 261–304.

Marusic, I., McKeon, B. J., Monkewitz, P. A., Nagib, H. M., Smits, A. J., Sreenivasan, K. R., 2010. Wall-bounded turbulent flows at high Reynolds numbers: Recent advances and key issues. Physics of Fluids 22 (6), 065103.

Mathis, R., Hutchins, N., Marusic, I., 2009. Large-scale amplitude modulation of the small-scale structures in turbulent boundary layers. Journal of Fluid Mechanics 628, 311–337.

Mathis, R., Marusic, I., Hutchins, N., Sreenivasan, K. R., 2011. The relationship between the velocity skewness and the amplitude modulation of the small scale by the large scale in turbulent boundary layers. Physics of Fluids 23 (12), 121702.

Nozu, T., Tamura, T., 2012. LES of turbulent wind and gas dispersion in a city. Journal of Wind Engineering and Industrial Aerodynamics 104-106, 492–499.

Oke, T. R., 1988. Street design and urban canopy layer climate. Energy and Buildings 11 (1), 103–113.

Otte, T. L., Lacser, A., Dupont, S., Ching, J. K. S., 2004. Implementation of an Urban Canopy Parameterization in a Mesoscale Meteorological Model. Journal of Applied Meteorology and Climatology 43 (11), 1648–1665.

Penelon, T., Calmet, I., Mironov, D. V., 2001. Micrometeorological simulations over a complex terrain witj submeso : a model study using a novel pre-processor. Int. J. Env. Poll. 16, 583–602.

Perret, L., Basley, J., Mathis, R., Thibaud, P., 2019. The atmospheric boundary layer over urban-like terrain: Influence of the plan density on roughness sublayer dynamics. Boundary-Layer Meteorol 170.

Perret, L., Kerhervé, F., 2019. Identification of very large scale structures in the boundary layer over large roughness elements. Exp Fluids 60.

Perret, L., Patton, E. G., 2021. Stability influences on interscale transport of turbulent kinetic energy and Reynolds shear stress in atmospheric boundary layers interacting with a tall vegetation canopy. Journal of Fluid Mechanics 921, A14.

Perret, L., Rivet, C., 2018. A priori analysis of the performance of cross hot-wire probes in a rough wall boundary layer based on stereoscopic PIV. Exp Fluids 59 (10), 153.

Perry, A. E., Marušić, I., 1995. A wall-wake model for the turbulence structure of boundary layers. Part 1. Extension of the attached eddy hypothesis. Journal of Fluid Mechanics 298, 361–388.

Placidi, M., Ganapathisubramani, B., 2015. Effects of frontal and plan solidities on aerodynamic parameters and the roughness sublayer in turbulent

boundary layers. Journal of Fluid Mechanics 782, 541–566.

Potsis, T., Tominaga, Y., Stathopoulos, T., 2023. Computational wind engineering: 30 years of research progress in building structures and environment. Journal of Wind Engineering and Industrial Aerodynamics 234, 105346.

Raupach, M., Finnigan, J., Brunet, Y., 1996. Coherent eddies and turbulence in vegetation canopies: The mixing-layer analogy. Boundary-Layer Meteorology 78, 351–382.

Raupach, M. R., Antonia, R. A., Rajagopalan, S., 1991. Rough-Wall Turbulent Boundary Layers. Applied Mechanics Reviews 44 (1), 1–25.

Raupach, M. R., Shaw, R. H., 1982. Averaging procedures for flow within vegetation canopies. Boundary-Layer Meteorology 22 (1), 79–90.

Reynolds, R. T., Castro, I. P., 2008. Measurements in an urban-type boundary layer. Experiments in Fluids 45 (1), 141–156.

Salesky, S. T., Anderson, W., 2018. Buoyancy effects on large-scale motions in convective atmospheric boundary layers: implications for modulation of near-wall processes. Journal of Fluid Mechanics 856, 135–168.

Santiago, J. L., Coceal, O., Martilli, A., Belcher, S. E., 2008. Variation of the Sectional Drag Coefficient of a Group of Buildings with Packing Density. Boundary-Layer Meteorology 128 (3), 445–457.

Santiago, J. L., Martilli, A., 2010. A Dynamic Urban Canopy Parameterization for Mesoscale Models Based on Computational Fluid Dynamics Reynolds-Averaged Navier–Stokes Microscale Simulations. Boundary-Layer Meteorol 137 (3), 417–439.

Shaw, R. H., Schumann, U., 1992. Large-eddy simulation of turbulent flow above and within a forest. Boundary-Layer Meteorol 61 (1), 47–64.

Thordal, M. S., Bennetsen, J. C., Koss, H. H. H., 2019. Review for practical application of CFD for the determination of wind load on high-rise buildings. Journal of Wind Engineering and Industrial Aerodynamics 186, 155–168.

Tolias, I. C., Koutsourakis, N., Hertwig, D., Efthimiou, G. C., Venetsanos, A. G., Bartzis, J. G., 2018. Large Eddy Simulation study on the structure of turbulent flow in a complex city. Journal of Wind Engineering and Industrial Aerodynamics 177, 101–116.

Townsend, A. A., 1976. The structure of turbulent shear flow, 2nd Edition. Cambridge monographs on mechanics and applied mathematics. Cambridge University Press, Cambridge [Eng.] ; New York.

Varghese, J., Durbin, P. A., 2020. Representing surface roughness in eddy resolving simulation. Journal of Fluid Mechanics 897, A10.

Wang, J., Li, C., Huang, S., Zheng, Q., Xiao, Y., Ou, J., 2023. Large eddy simulation of turbulent atmospheric boundary layer flow based on a synthetic volume forcing method. Journal of Wind Engineering and Industrial Aerodynamics 233, 105326.

Watanabe, T., 2004. Large-eddy simulation of coherent turbulence structures associated with scalar ramps over plant canopies. Boundary-Layer Meteorology 112 (2), 307–341.

Wilson, N. R., Shaw, R. H., 1977. A Higher Order Closure Model for Canopy Flow. Journal of Applied Meteorology and Climatology 16 (11), 1197–1205.

Xue, M., Droegemeier, K. K., Wong, V., 2000. The Advanced Regional Prediction System (ARPS) – A multi-scale nonhydrostatic atmospheric simulation and prediction model. Part I: Model dynamics and verification. Meteorol Atmos Phys 75 (3), 161–193.

Xue, M., Droegemeier, K. K., Wong, V., Shapiro, A., Brewster, K., Carr, F., Weber, D., Liu, Y., Wang, D., 2001. The Advanced Regional Prediction System (ARPS) – A multi-scale nonhydrostatic atmospheric simulation and prediction tool. Part II: Model physics and applications. Meteorol Atmos Phys 76 (3), 143–165.

Yang, X. I. A., Sadique, J., Mittal, R., Meneveau, C., 2016. Exponential roughness layer and analytical model for turbulent boundary layer flow over rectangular-prism roughness elements. Journal of Fluid Mechanics 789, 127–165.

Yue, W., Parlange, M., Meneveau, C., Zhu, W., van Hout, R., Katz, J., 2007. Large-eddy simulation of plant canopy flows using plant-scale representation. Boundary-Layer Meteorology 124.